Received: Added at production | Revised: Added at production | Accepted: Added at production

DOI: xxx/xxxx

ARTICLE TYPE

Hybrid equilibrium formulation with adaptive element side orientation for cohesive crack prediction

Francesco Parrinello

Engineering Department, University of Palermo, Viale delle Scienze, Ed. 8, 90128 Palermo, Italy

Correspondence
Email: francesco.parrinello@unipa.it

Summary

The present paper proposes an Hybrid Equilibrium Element (HEE) formulation for the prediction of cohesive fracture formation and propagation with the crack modelled by extrinsic interface embedded at element sides. The hybrid equilibrium element formulation can model high order (quadratic, cubic and quartic) stress fields which strongly satisfy homogeneous equilibrium equations, inter-element and boundary equilibrium equations. The HEE can implicitly model both the initially rigid behaviour of an extrinsic interface and its debonding condition with separation displacement and softening. The extrinsic interface is embedded at the element sides and its behaviour is governed by means of the same degrees of freedom of HEE (*generalized stresses*), without any additional degree of freedom. The proposed extrinsic cohesive model is developed in the thermodynamic framework of damage mechanics. The proposed crack propagation criterion states that crack grows when the maximum principal stress reaches the tensile strength value, in a direction orthogonal to the principal stress direction. The crack is embedded at an element side and the mesh around crack tip is adapted, by rotation of the element sides, in order to have the interface aligned to the crack growth direction. Three classic two-dimensional problems of fracture propagation are numerically reproduced and the results compared to the experimental data or to the other numerical results.

KEYWORDS:
Extrinsic Interface, Inter-element fracture, HEE, remeshing

1 | INTRODUCTION

The mechanical behaviour of brittle and quasi-brittle materials under tensile stress is characterized by irreversible micro-mechanical phenomena such as diffuse damage, oriented micro-cracking and fracture, which can dangerously degenerate to material failure and to the collapse of structural elements. Many approaches have been developed for modelling and for the numerical simulation of fracture propagation phenomena, and most of them can be framed in the continuum damage mechanics or in the discrete crack models. Classic continuum damage models are susceptible of localization phenomena with pathological mesh dependency, which can be faced by regularization techniques such as the gradient or non-local formulations [1,2,3] or, following a recent trend, by phase-field damage models [4,5]. In continuum damage mechanics the crack pattern is not postulated a priori neither explicitly modelled, whereas in discrete crack formulations the location of the crack path is geometrically defined as a potential separation surface within the solid, where a discontinuity in displacement field is explicitly modelled.

The discrete crack (DC) can be modelled by zero-thickness interface elements with their own nonlinear constitutive equations. When the failure surface is *a priori* known, such as the delamination surface of composite materials, interface elements need to be inserted following the FE mesh conforming to the potential discontinuity surface. More flexible formulations for crack modelling are the strong or embedded discontinuity (EFEM) approaches[6,7,8,9] and the eXtended-generalized FEM (XFEM, GFEM)[10,11,12], which enable crack propagation with arbitrary path across the elements, without re-meshing. The two different approaches of discrete crack modelling (EFEM and XFEM) are compared by Oliver et al in Ref.[13].

The crack path can be predicted by discrete formulation in the framework of linear Elastic Fracture Mechanics (LEFM) by evaluation of stress intensity factors (SIFs)[14], strain energy release rates (SERRs)[15] or by the well known J-integral method[16,17]. An alternative approach is the so called Cohesive Fracture Mechanics (CFM), which combines the DC kinematic formulation with Cohesive Zone Models (CZM). The CZMs describe the Traction Separation Law (TSL) at the discontinuity surface and, as pointed out since the pioneering works of Dugdale[18] and Barenblatt[19], allow us to overcome the mathematical issue of the stress singularity ahead of the crack tip of LEFM[20]. The constitutive modelling of the separation surface has been thoroughly investigated from several point of view, such as: isotropy and orthotropy behaviours[21], coupled damage-plastic[22], independent mode I and mode II fracture toughness[23,24,25], thermodynamic consistency[26,27,28], cohesive-frictional behaviour[29,26], finite displacement conditions[23,30] etc. The references here cited represent a short and largely incomplete review of the huge literature on interface constitutive models.

Most of the available CZMs are defined as intrinsic, assuming an elastic behaviour in the pre-failure regime, with a reversible separation between the two edges of the discontinuity surface for tensile and tangential traction values lower then interface strength. The elastic separation generally is not a mechanical deformation but the approximation given by the penalty method, which is applied to keep joined the two connected bodies in both the opening and closure conditions. Drawback of the penalty method is the additional and artificial compliance which alters the body elastic response and can produce spurious traction oscillations at the crack tip[31] end error in the evaluation of wave speed in dynamic analysis.

The extrinsic TSLs, as opposed to intrinsic ones, models an initial rigid behaviour, with perfect adhesion of the two edges of separation surface for traction lower then interface strength. Extrinsic models overcome the above mentioned drawbacks of intrinsic models and are appealing in the modelling of crack propagation. However, the coupling of an extrinsic interface with a displacement based finite element formulation for the analysis of cohesive crack is not straightforward and it requires some special numerical treatment, such as the Discontinuous Galerkin (DG) method proposed in Ref.[32], which weakly enforces the displacement continuity at the interface by application of Nitsche's method[33]. Nitsche's method, in the form of DG and coupled with an extrinsic TSL, is also the numerical resolution strategy adopted in Ref.[34] for the analysis of interfacial cracking between non-matching meshes, for debonding analysis in composite materials Ref.[35], or for intergranular degradation and failure in polycrystalline materials through the boundary element method in Refs.[36,37]. The DG method coupled with an extrinsic TSL is adopted in Ref.[38] for static and dynamic analysis of interface separation, and the results are compared to the intrinsic interface formulation, showing significant improvement in evaluation of the wave speed. In Refs.[39,40] the dynamic crack propagation on an arbitrary path has been modelled by the DG method with extrinsic TSL. An alternative approach for the modelling of an extrinsic TSL in a known crack path with FEM is proposed in Ref.[41] and is based on a mixed formulation through which the perfect adhesion at the interface is enforced and the cohesive tractions are assumed as Lagrangian variables. The main drawbacks of all such formulations for the analysis of crack propagation phenomenon are: the mesh generation, which requires an interface element inserted at every inter-element boundary and independent nodes for each element; the mesh dependency of crack path, which can be mitigated by mesh refinement.

More recently, the analysis of cohesive crack propagation at the inter-element interface has been faced by the author in Ref.[42] by mean of the Hybrid Equilibrium Element (HEE) formulation, which can implicitly embed an extrinsic interface at any element side with neither additional degree of freedom, nor additional nodes, and without any remeshing. HEE provides a very accurate solution of the elastic problem employing higher order stress fields, namely: quadratic, cubic or quartic, which strongly satisfy the homogeneous equilibrium equations and inter-element and boundary equilibrium equations[43,44,45,46,47,48]. Embedded interface can model perfect adhesion at the pristine condition and a linear softening, with active separation between the edges of interface, when activation condition is attained. Interface behaviour is modelled as an extrinsic TSL developed in a the thermodynamic framework of damage mechanics. The HEE formulation was also extended to the dynamic analysis of elastic solids in Ref.[49].

The stress based formulation developed in Ref.[42] can be considered an effective alternative for the analysis of fracture propagation. However, the approach proposed in Ref.[42] models the inter-element crack through a fixed mesh and with a mixed mode crack opening criterion, which is governed both by the tensile traction component and by the tangential one. As a consequence, it is not immune to mesh dependence of the crack trajectory and the overall response is strongly affected by the mesh size and

orientation chosen for the non linear analysis. In present paper the formulation proposed by the author in Ref.[42] for the inter-element crack propagation is significantly improved and the most relevant novelty are the crack propagation criterion and the remeshing of elements ahead of the crack tip. In detail, the criterion assumed for determining the crack propagation direction is that of the maximum principal stress, which can be considered the most suitable criterion for a stress based approach, at least for isotropic materials. The crack grows when the maximum principal stress σ_1 reaches the tensile strength value s_0 and the crack propagates in the direction orthogonal to the principal stress direction, which generally does not coincides to any element side. Therefore, the mesh around crack tip has to be adapted to the direction of crack propagation, by rotation of the element sides, so that the embedded interface is aligned to the crack growth direction. Finally, the resolution approach of the nonlinear problem of damage evolution, which cannot be solved at the single Gauss point level but for the whole element with embedded interface, is improved and simplified.

The paper is organized as follows: the HEE is developed in Section 2. The HEE with an interface embedded at one element side and the extrinsic TSL are proposed in Section 3. The crack propagation criterion and the remeshing of elements ahead of the crack tip are presented in Section 4. The results of the numerical simulations are reported in Section 5 and, finally, closing remarks are given in Section 6.

2 | HYBRID EQUILIBRIUM ELEMENT FORMULATION

Let us consider a 2D elastic body occupying the closed region Ω. The body is referred to a Cartesian reference system (x, y) and each point $\boldsymbol{x}$ is subjected to vector field body force $\boldsymbol{b}(\boldsymbol{x}, \tau)$ in Ω , vector traction $\boldsymbol{t}(\boldsymbol{x}, \tau)$ on the free boundary Γ_T, imposed vector displacement $\overline{\mathbf{u}}(\boldsymbol{x}, \tau)$ on the constrained boundary Γ_U at each time $\tau \in (t_0, t)$. The equilibrium formulation belongs to the class of stress-based approaches and the weak form solution of the elasto-static problem is given as stationary condition of the complementary energy functional, with stress satisfying the domain and boundary equilibrium equations.

Mixed and hybrid formulations can be encompassed in the more general framework of multifield finite element methods (see Ref.[50] for more details). Mixed elements are, generally, conforming with continuous displacement interpolating nodal values. Stress fields are discontinuous and satisfy equilibrium equation only weakly. Solution of elastic problems for such elements is generally given as stationary condition of the Hellinger-Reissner functional. Conversely, hybrid equilibrium elements are not conforming and are based con stress fields which strongly satisfy equilibrium equations. The solution of elastic problems is given as stationary condition of the complementary energy functional and displacement field plays the role of Lagrangian variable.

The two-dimensional static equilibrium formulation considered in the present paper follows the same reasoning path as proposed in Refs.[51,42] and the following assumptions are considered:

- The two-dimensional solid continuum domain Ω is discretized by a set $\mathcal{E}$ of non-overlapping triangular subdomains Ω_e, with $e \in \mathcal{E}$, such that $\Omega = \bigcup_{e\in\mathcal{E}} \Omega_e$.
- The set of all element sides is denoted by $\mathcal{B} = \mathcal{B}_T \cup \mathcal{B}_U \cup \mathcal{B}_{int}$ where $\mathcal{B}_T$ is the set of external free boundary element sides, $\mathcal{B}_U$ is the set of constrained boundary sides and $\mathcal{B}_{int}$ is the set of internal element sides (inter-element sides).
- The set of three sides of element e is denoted by $\mathcal{B}_e = (s_1, s_2, s_3) \subset \mathcal{B}$ and the element subdomain boundary $\Gamma^e \equiv \partial\Omega_e = \bigcup_{s\in\mathcal{B}_e} \Gamma_s$ is composed of three sides $\Gamma_i^e = \Gamma_{s_i}$ with $s_i \in \mathcal{B}_e$ and $i = 1, 2, 3$.
- Each element side can lie at the free boundary $\Gamma_s \subset \Gamma_T$ and $s \in \mathcal{B}_T$, or can lie at the constrained boundary $\Gamma_s \subset \Gamma_U$ and $s \in \mathcal{B}_U$, or can be an internal side between two subdomains $\Gamma_s \equiv \partial\Omega e_1 \cap \partial\Omega e_2$, with $e_1 \neq e_2$ and $s \in \mathcal{B}_{int}$.
- The set of integration points of the side Γ_i^e is denoted by $\mathcal{G}_i^e$, that is: $\boldsymbol{x}_g \in \Gamma_i^e$ with $g \in \mathcal{G}_i^e$.
- The subset of active integration points, that are points $\boldsymbol{x}_g \in \Gamma_i^e$ with increasing damage $\dot{\omega}_g > 0$, is denoted by $\mathcal{D}_i^e \cup \mathcal{G}_i^e$.
- The subset of fully damaged integration points, that are points $\boldsymbol{x}_g \in \Gamma_i^e$ with damage $\omega_g = 1$, is denoted by $\mathcal{L}_i^e \cup \mathcal{G}_i^e$.

The element sides Γ_s with $s \in \mathcal{B}$ can be curved and the hybrid approach of the equilibrium formulation is developed with the stress fields $\boldsymbol{\sigma}_e$ independently defined and satisfying the equilibrium equation in each subdomain ($\operatorname{div}\boldsymbol{\sigma}_e + \boldsymbol{b}_e = \mathbf{0}$ in Ω_e). The inter-element equilibrium condition at all internal sides and the boundary equilibrium condition at all free boundary sides are imposed by the classical hybrid formulation, for which independent displacement field $\boldsymbol{u}_s(\boldsymbol{x})$ with $\boldsymbol{x} \in \Gamma_s$ is defined for each element side $s \in \mathcal{B}$, and is assumed as Lagrangian variable in order to mutually connect adjacent elements or to apply traction

on the free boundary (see for example Refs.[46,52,48,51,42]). For the triangular finite element discretization, the hybrid equilibrium formulation gives the following modified complementary energy functional:

$$\overline{\Pi}_c\left(\sigma_{e\in\mathcal{E}}, \boldsymbol{u}_{s\in\mathcal{B}_e}\right) = \sum_{e\in\mathcal{E}} \frac{1}{2}\int_{\Omega_e} \boldsymbol{\sigma}_e : \mathbf{D} : \boldsymbol{\sigma}_e \, d\Omega - \sum_{\substack{e\in\mathcal{E}\\ s\in\mathcal{B}_e}} \int_{\Gamma_s} \boldsymbol{n}_s^e \cdot \boldsymbol{\sigma}_e \cdot \boldsymbol{u}_s \, d\Gamma + \sum_{s\in\mathcal{B}_T} \int_{\Gamma_s} \boldsymbol{t}\cdot\boldsymbol{u}_s \, d\Gamma \tag{1}$$

with $\boldsymbol{u}_s \equiv \overline{\boldsymbol{u}}$ on constrained sides $s \in \mathcal{B}_U$ and $\boldsymbol{n}_s^e$ the outward unit vector normal to side $\Gamma_s \subset \partial\Omega_e$.

The stationary condition of the functional $\overline{\Pi}_c$, with respect to the Lagrangian variable $\boldsymbol{u}_s$ gives the weak form of the inter-element equilibrium condition for an internal side and the weak form of the boundary equilibrium condition for a free boundary side. The stationary conditions of the functional $\overline{\Pi}_c$, with respect to the stress tensor $\boldsymbol{\sigma}_e$ provides a weak form of the compatibility condition between elastic strains $\boldsymbol{\varepsilon}_e \equiv \mathbf{D} : \boldsymbol{\sigma}_e$ and displacement at the boundary sides $\boldsymbol{u}_s$ with $s \in \mathcal{B}_e$. Details of the static formulation are given in Refs.[51,42].

In hybrid equilibrium formulations the finite element is defined by the element stress fields satisfying the domain equilibrium equation, which does not interpolate nodal degrees of freedom, but are functions of *generalized stresses*. In the present paper, the hybrid equilibrium element is developed only for two-dimensional membrane problems with polynomial stress fields of order $n_s = 2, 3, 4$.

Let a triangular Hybrid Equilibrium Element (HEE) of domain Ω_e be considered and referred to a local Cartesian reference (x, y) centred at vertex 1, as shown in Figs. 1a-c. The quadratic stress fields ($n_s = 2$) of a two-dimensional element are defined by the following polynomial functions

$$\sigma_x(x,y) = a_1 + a_2 y + a_3 y^2 - a_9 x - a_{10}x^2/2 - 2a_{12}xy - b_x, \tag{2}$$

$$\sigma_y(x,y) = a_4 + a_5 x + a_6 x^2 - a_8 y - a_{10}y^2/2 - 2a_{11}xy - b_y, \tag{3}$$

$$\tau_{xy}(x,y) = a_7 + a_8 x + a_9 y + 2a_{10}xy + a_{11}x^2 + a_{12}y^2, \tag{4}$$

where, b_x and b_y are components of uniform volume force vectors acting on the element, and terms $a_1, \ldots, a_{12}$ are *generalized stress* variables. The stress fields of Eqs.(2-4) implicitly satisfy the domain equilibrium equation and for the $e-th$ element can be represented in the following Voigt notation

$$\boldsymbol{\sigma}_e(\boldsymbol{x}) = \mathbf{S}_e(\boldsymbol{x})\mathbf{a}_e + \boldsymbol{\sigma}_e^0 \;\text{ with }\; \boldsymbol{x} \in \Omega_e \tag{5}$$

where $\mathbf{S}_e(\boldsymbol{x})$ is the stress modelling matrix, vector $\mathbf{a}_e$ (of dimension $n_a = 12$) collects all *generalized stress* variables, $\boldsymbol{\sigma}_e^0 = \left[-b_x, -b_y, 0\right]^T$ is a particular solution of the domain equilibrium equation, due to a uniform body force, and $\boldsymbol{\sigma}_e = \left[\sigma_x^e, \sigma_y^e, \tau_{xy}^e\right]^T$. The proposed formulation still satisfies the equilibrium equations if non-uniform body forces are considered, but only with polynomial function of order lower than that of stress formulation. The cubic and quartic stress fields are analogously defined and the dimension of *generalized stress* vector $\mathbf{a}_e$ is $n_a = 18$ for the cubic stress and $n_a = 24$ for the quartic one. See AppendixA for the respective forms of the matrix $\mathbf{S}_e(\boldsymbol{x})$ and vector $\mathbf{a}_e$ in the quadratic, cubic and quartic stress field formulations.

Displacement is independently defined at each element side and continuity at the vertexes is not strongly imposed. In the proposed stress-based approach, equilibrium condition is pointwise satisfied, whereas displacement continuity can only be weakly imposed. The geometry and displacement of all element sides Γ_s are modelled by a classic isoparametric mapping

$$\boldsymbol{x}_s(\xi) = \mathbf{N}(\xi)\,\mathbf{x}_s\,, \tag{6}$$

$$\boldsymbol{u}_s(\xi) = \mathbf{N}(\xi)\,\mathbf{u}_s\,, \tag{7}$$

where $\mathbf{N}(\xi)$ is the matrix collecting the shape functions and the vectors $\mathbf{x}_s$, $\mathbf{u}_s$ collect respectively coordinates and kinematic degrees of freedom of side Γ_s.

The complementary energy functional $\overline{\Pi}_c$ in Eq.(1) can be rewritten in the following discretized form

$$\overline{\Pi}_c = \sum_{e\in\mathcal{E}} \left[\frac{1}{2}\mathbf{a}_e^T\mathbf{C}_e\mathbf{a}_e - \mathbf{a}_e^T\mathbf{H}_e\mathbf{u}_e + \mathbf{T}_e^T\mathbf{u}_e\right], \tag{8}$$

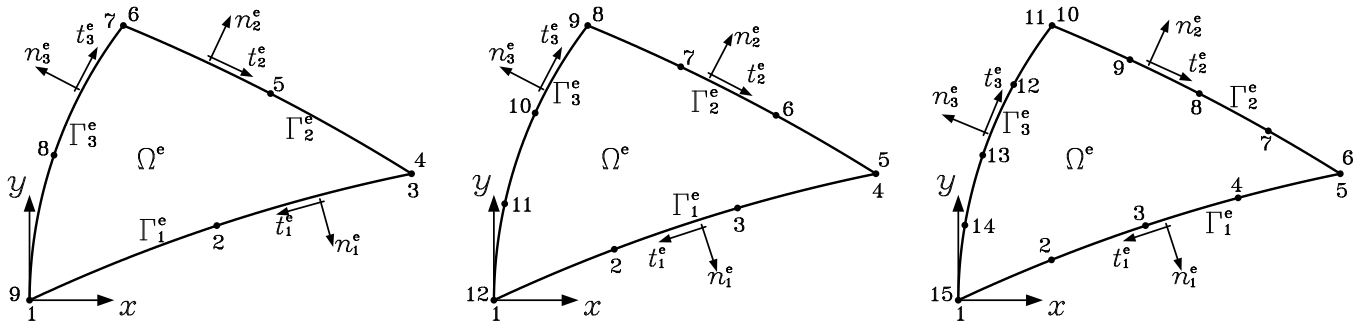

FIGURE 1 Nine-node, twelve-node and fifteen-node triangular Hybrid Equilibrium Elements (HEE).

where

$$\mathbf{C}_e = \int_{\Omega_e} \mathbf{S}_e^T \mathbf{D}\, \mathbf{S}_e d\Omega, \tag{9}$$

$$\mathbf{H}_e = \left[\mathbf{h}_1^e, \mathbf{h}_2^e, \mathbf{h}_3^e\right] \text{ with } \mathbf{h}_i^e = \int_{\Gamma_i^e} \mathbf{S}_e^T \mathbf{n}_i^e\, \mathbf{N} d\Gamma, \tag{10}$$

$$\mathbf{T}_e = \left[\mathbf{t}_1^e, \mathbf{t}_2^e, \mathbf{t}_3^e\right] \text{ with } \mathbf{t}_i^e = \int_{\Gamma_i^e = \Gamma_{s_i}} \mathbf{N}^T \boldsymbol{t} d\Gamma \text{ and } s_i \in \mathcal{B}_e \cap \mathcal{B}_T, \tag{11}$$

$$\mathbf{u}_e = \left[\mathbf{u}_1^e, \mathbf{u}_2^e, \mathbf{u}_3^e\right] = \left[\mathbf{u}_{s_1}, \mathbf{u}_{s_2}, \mathbf{u}_{s_3}\right] \text{ and } s_i \in \mathcal{B}_e, \tag{12}$$

$$\mathbf{n}_i^e = \begin{bmatrix} n_{ix}^e & 0 \\ 0 & n_{iy}^e \\ n_{iy}^e & n_{ix}^e \end{bmatrix}. \tag{13}$$

The stationary conditions of the functional $\overline{\Pi}_c$ with respect to the Lagrangian variable $\mathbf{u}_s$ gives the weak form of inter-element equilibrium condition for an internal side $s \in \mathcal{B}_{int}$ and the weak form of boundary equilibrium condition $\mathbf{t}_s^e = \mathbf{h}_s^{eT} \mathbf{a}_e$ for a boundary side $s \in \mathcal{B}_e \cap \mathcal{B}_T$ (see Ref.[42] for details).

The stationary condition of functional $\overline{\Pi}_c$ in Eq.(8), with respect to the *generalized stress* vector $\mathbf{a}_e$, gives the following element equation of the discretized static hybrid equilibrium formulation

$$\frac{\partial \overline{\Pi}_c}{\partial \mathbf{a}_e} = \mathbf{C}_e \mathbf{a}_e - \mathbf{H}_e \mathbf{u}_e = \mathbf{C}_e \mathbf{a}_e - \mathbf{h}_1^e \mathbf{u}_1^e - \mathbf{h}_2^e \mathbf{u}_2^e - \mathbf{h}_3^e \mathbf{u}_3^e = \mathbf{0}, \tag{14}$$

which states the relationship between nodal displacement and *generalized stress* variables at the element level. The element nodal force vector can also be written as $\mathbf{q}_e = \mathbf{H}_e^T \mathbf{a}_e$ and the equation of the single hybrid equilibrium element is

$$\begin{bmatrix} \mathbf{C}_e & -\mathbf{H}_e \\ -\mathbf{H}_e^T & \mathbf{0} \end{bmatrix} \begin{bmatrix} \mathbf{a}_e \\ \mathbf{u}_e \end{bmatrix} = \begin{bmatrix} \mathbf{0} \\ -\mathbf{q}_e \end{bmatrix} \tag{15}$$

where the compliance matrix $\mathbf{C}_e$ is symmetric, positive definite and not singular, so that it can be inverted and the *generalized stress* vector $\mathbf{a}_e$ can be condensed out at the element level; that is, mathematically

$$\mathbf{a}_e = {\mathbf{C}_e}^{-1} \mathbf{H}_e \mathbf{u}_e \tag{16}$$

$$\mathbf{q}_e = \mathbf{H}_e^T {\mathbf{C}_e}^{-1} \mathbf{H}_e \mathbf{u}_e = \mathbf{K}_e \mathbf{u}_e \tag{17}$$

where the matrix $\mathbf{K}_e = \mathbf{H}_e^T {\mathbf{C}_e}^{-1} \mathbf{H}_e$ is the element stiffness matrix and the HEE can be implemented in a classic displacement-based finite element code. Vector $\mathbf{q}_e = \left[\mathbf{q}_1^e, \mathbf{q}_2^e, \mathbf{q}_3^e\right]$ collects the nodal forces of the three element sides and such forces coincide to the boundary traction forces for a boundary side, that is $\mathbf{q}_s^e = \mathbf{t}_s^e = \mathbf{h}_s^{eT} \mathbf{a}_e$ for side $s \in \mathcal{B}_e \cap \mathcal{B}_T$.

The use of the same order for the stress fields and for displacement of side ($n_s = n_d$) allows the proposed formulation to accurately verify the inter-element equilibrium condition, with co-diffusive stresses $\boldsymbol{\sigma}_{e_1}$ and $\boldsymbol{\sigma}_{e_2}$ through the inter-element side

$\Gamma_{int} = \partial\Omega_{e_1} \cap \partial\Omega_{e_2}$. Therefore, in order to impose the inter-element equilibrium condition, the nine-node HEE in Fig. 1a is employed with a quadratic stress field, while the twelve-node HEE in Fig. 1b is employed with a cubic stress field and the fifteen-node HEE in Fig. 1c is employed with a quartic stress field. The inter-element equilibrium condition at internal sides and boundary equilibrium condition at external sides are strongly satisfied only for straight sides, whereas are weakly imposed for curved sides.

3 | HEE WITH EMBEDDED EXTRINSIC INTERFACE

The hybrid equilibrium element, with its property of independent displacement fields for each side, is particularly suitable for modelling of decohesion along an element side, without any additional degree of freedom. For the sake of clarity let us initially consider an interface Γ_0 inserted into the two-dimensional elastic domain Ω so that $\Gamma_0 \cup \Omega$ and $\Gamma_0 \cap \partial\Omega = 0$. The domain discretization is defined in such a way that no one HEE is crossed by the interface and the interface is discretized by the set $\mathcal{B}_0 \cup \mathcal{B}_{int}$ of internal element sides, that is: $\Gamma_0 = \bigcup_{s\in\mathcal{B}_0} \Gamma_s$. From the kinematic point of view the interface behaviour is modelled by the jump or separation displacement between the positive and negative edges of the interface, that is $\boldsymbol{e} := [\![\boldsymbol{u}]\!] = \boldsymbol{u}^+ - \boldsymbol{u}^-$. The behaviour is initially modelled as linear elastic by the following relationship between traction components $\mathbf{s} = \boldsymbol{\sigma}\boldsymbol{n}_0$, with $\boldsymbol{n}_0$ the unit vector normal to the interface Γ_0, and the separation displacement

$$\boldsymbol{e} = \mathbf{A}^{el}\mathbf{s}, \tag{18}$$

where $\mathbf{A}^{el}$ is the interface compliance diagonal matrix. The elastic interface introduces an additional elastic strain energy contribution in the complementary energy functional in Eq.(1) which is given as

$$\overline{\Pi}_c = \sum_{e\in\mathcal{E}} \frac{1}{2}\int_{\Omega_e} \boldsymbol{\sigma}_e : \mathbf{D} : \boldsymbol{\sigma}_e \, d\Omega + \sum_{s\in\mathcal{B}_0} \frac{1}{2}\int_{\Gamma_s} \mathbf{s}\cdot\mathbf{A}^{el}\cdot\mathbf{s}\, d\Gamma - \sum_{\substack{e\in\mathcal{E}\\ s\in\mathcal{B}_e}} \int_{\Gamma_s} \boldsymbol{n}_s^e\cdot\boldsymbol{\sigma}_e\cdot\boldsymbol{u}_s\, d\Gamma + \sum_{s\in\mathcal{B}_T}\int_{\Gamma_s} \boldsymbol{t}\cdot\boldsymbol{u}_s\, d\Gamma \tag{19}$$

In the proposed HEE formulation the interface is embedded at the element side and the relevant traction can be modelled as function of the same vector $\mathbf{a}_e$ of *generalized stress* variables as adopted for the stress functions in Eqs.(2-5) of the HEE. For an interface embedded at the side Γ_1^e with normal $\mathbf{n}_1^e$ (outward from the *e-th* finite element and defined in Voigt notation in Eq.(13), the traction vector in equilibrium with element stress fields can be defined in the following Voigt notation

$$\boldsymbol{s}(\boldsymbol{x}) = \mathbf{n}_1^{eT}\boldsymbol{\sigma}_e(\boldsymbol{x}) = \mathbf{n}_1^{eT}\mathbf{S}_e(\boldsymbol{x})\,\mathbf{a}_e \quad \text{with} \quad \boldsymbol{x}\in\Gamma_1^e\subset\Gamma_0. \tag{20}$$

and the complementary energy functional in Eq.(19) can be written in the following discretized form

$$\overline{\Pi}_c = \sum_{e=1}^{n_e}\left[\frac{1}{2}\mathbf{a}_e^T\left(\mathbf{C}_e + \mathbf{C}_e^{\Gamma}\right)\mathbf{a}_e - \mathbf{a}_e^T\mathbf{H}_e\mathbf{u}_e + \mathbf{T}_e^T\mathbf{u}_e\right], \tag{21}$$

where

$$\mathbf{C}_e^{\Gamma} = \int_{\Gamma_1^e\subset\Gamma_0} \mathbf{S}_e^T\mathbf{n}_1^e\,\mathbf{A}^{el}\mathbf{n}_1^{eT}\mathbf{S}_e d\Gamma. \tag{22}$$

is the additional compliance matrix due to the embedded elastic interface. The embedded elastic interface at side Γ_1^e modifies the equation of the single HEE, defined in Eq.(15), with the additional interface compliance matrix $\mathbf{C}_e^{\Gamma}$ and Eq.(15) becomes

$$\begin{bmatrix}\mathbf{C}_e + \mathbf{C}_e^{\Gamma} & -\mathbf{H}_e\\ -\mathbf{H}_e^T & \mathbf{0}\end{bmatrix}\begin{bmatrix}\mathbf{a}_e\\ \mathbf{u}_e\end{bmatrix} = \begin{bmatrix}\mathbf{0}\\ -\mathbf{q}_e\end{bmatrix} \tag{23}$$

and the *generalized stress* vector and the nodal force vector are given as

$$\mathbf{a}_e = \left(\mathbf{C}_e + \mathbf{C}_e^{\Gamma}\right)^{-1}\mathbf{H}_e\mathbf{u}_e \tag{24}$$

$$\mathbf{q}_e = \mathbf{H}_e^T\left(\mathbf{C}_e + \mathbf{C}_e^{\Gamma}\right)^{-1}\mathbf{H}_e\mathbf{u}_e = \mathbf{K}_e\mathbf{u}_e, \tag{25}$$

where the matrix $\mathbf{K}_e = \mathbf{H}_e^T\left(\mathbf{C}_e + \mathbf{C}_e^{\Gamma}\right)^{-1}\mathbf{H}_e$ is the stiffness matrix of the HEE with embedded elastic interface.

In the proposed formulation the elastic interface can be embedded at one or more sides of an hybrid equilibrium element without any additional degrees of freedom, simply considering the additional interface compliance matrix $\mathbf{C}_e^{\Gamma}$ defined in Eq.(22).

3.1 | Extrinsic interface

The HEE formulation with embedded interface is also particularly effective for modelling an extrinsic interface, which gives null separation displacement for the pristine interface. The extrinsic interface with a rigid-damage cohesive zone model (CZM) has been applied by the use of a discontinuous Galerkin method in Refs.[32,40,53,54] for numerical analysis of delamination phenomena and for analysis of crack propagation. The discontinuous Galerkin method is also proposed in Ref.[34] for interfacial cracking with extrinsic interface combined with non-matching discretization of the domains.

The extrinsic interface is modelled in the present paper by the rigid-damage CZM proposed by the Author in Refs.[42,55,56] in the rigorous thermodynamic framework of damage mechanics. The CZM is hereafter developed in a complementary form starting from the following Gibbs free energy function, defined for a unit of interface surface,

$$G(\boldsymbol{s},\omega)=\frac{1}{2}\frac{\omega}{1-\omega}\boldsymbol{s}^T\mathbf{A}^{el}\boldsymbol{s} \tag{26}$$

where $0\leq\omega\leq 1$ is the scalar damage variable. The interface elastic compliance matrix is diagonal and defined as $A^{el}_{ij}=\delta_{ij}/k_0$ with δ_{ij} being the Kronecker delta and k_0 a stiffness parameter.

Thermodynamic consistency, in the form of the second principle, is enforced by the Clausius–Duhem inequality in the form of non-negative mechanical energy dissipation density, which can be formulated both in terms of Helmholtz free energy density and in terms of the Gibbs energy, that is

$$D=\boldsymbol{s}\cdot\dot{\boldsymbol{e}}-\dot{\Psi}=\dot{G}-\dot{\boldsymbol{s}}\cdot\boldsymbol{e}\geq 0 \tag{27}$$

where Helmholtz free energy density is the Legendre transformation of Gibbs energy, that is $\Psi(\boldsymbol{e},\omega)=\boldsymbol{s}\cdot\boldsymbol{e}-G(\boldsymbol{s},\omega)$. Considering the specific expression of Gibbs energy in Eq.(26)), upon expansion of the term $\dot{G}$ and after substitution of Eqs.(31 - 29), Eq. (27) yields

$$D=\frac{\partial G}{\partial\boldsymbol{s}}\dot{\boldsymbol{s}}+\frac{\partial G}{\partial\omega}\dot{\omega}-\dot{\boldsymbol{s}}\cdot\boldsymbol{e}\geq 0. \tag{28}$$

Purely elastic processes are reversible and non-dissipative and the absence of damage increments $\dot{\omega}=0$ implies that

$$\boldsymbol{e}:=\frac{\partial G}{\partial\boldsymbol{s}}=\frac{\omega}{1-\omega}\mathbf{A}^{el}\boldsymbol{s} \tag{29}$$

which defines the separation displacement $\boldsymbol{e}$ as the conjugate variable of interface traction $\boldsymbol{s}$ and Eq.(29) states the traction-separation law of the rigid-damage interface. Processes with increasing damage are dissipative and thermodynamic consistency imposes that

$$D=\frac{\partial G}{\partial\omega}\dot{\omega}=Y\dot{\omega}\geq 0. \tag{30}$$

where Y is the *energy release rate*, the conjugate variable of damage, and is obtained from Eq.(26)

$$Y:=\frac{\partial G}{\partial\omega}=\frac{1}{2}\frac{1}{(1-\omega)^2}\boldsymbol{s}\cdot\mathbf{A}^{el}\cdot\boldsymbol{s}. \tag{31}$$

3.1.1 | Damage activation condition

Thermodynamic consistency is enforced in the framework of damage mechanics and the following damage activation function is defined as

$$\phi(Y):=Y-Y_0\leq 0 \tag{32}$$

where Y_0 is the threshold for activation and evolution of damage, which coincides to the fracture energy G_I and is defined as

$$Y_0=G_I=\frac{s_0^2}{2k_0}=\frac{1}{2}k_0e_f^2 \tag{33}$$

being s_0 the interface strength and $e_f=s_0/k_0$ the separation displacement at the full debonding condition. The damage model is completed by the following associative flow rules and loading-unloading conditions

$$\dot{\omega}:=\frac{\partial\phi}{\partial Y}\dot{\lambda}=\dot{\lambda} \tag{34}$$

$$\dot{\lambda}\geq 0,\quad \phi\dot{\lambda}=0,\quad \dot{\phi}\dot{\lambda}=0. \tag{35}$$

through which an incremental a linear behaviour with null dissipation is modelled when $\phi<0$, whereas an incremental a non-linear behaviour with increasing damage and positive dissipation $D=Y\dot{\lambda}>0$ is obtained when the activation condition attains the limit condition $\phi=0$.

The proposed CZM is isotropic and produces a bilinear TSL with the same response in the pure opening condition, in the pure sliding, as represented in Figs.2a and b. Moreover, the two modes are fully coupled in the CZM for the dependence of the damage activation condition in Eq.(32) on the energy release rate Y, which is defined in Eq.(31) in terms of normal and tangential traction components. The model could be also extended to a more general formulation by a complementary formulation of the non-associative damage model proposed by the author in Ref.[25], in order to account for two different responses in pure mode I and in pure mode II loading conditions.

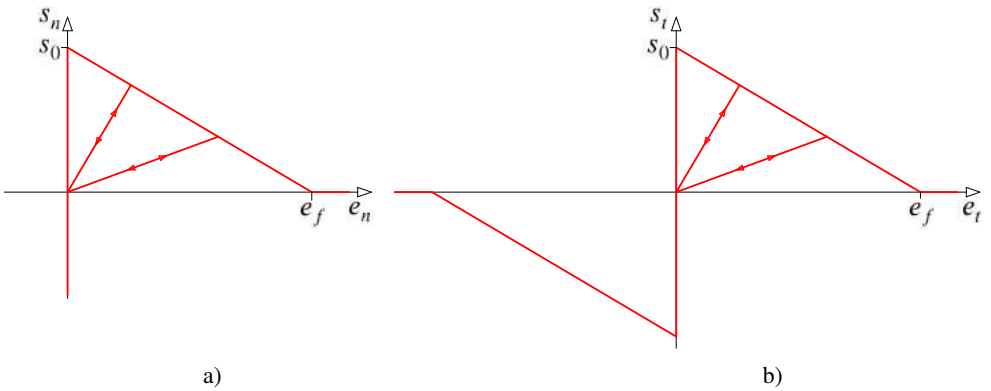

FIGURE 2 Bilinear response of the proposed extrinsic interface model with linear unloading-reloading conditions: a) pure opening mode with unlimited strength in compressive normal traction; b) pure sliding mode.

A HEE with embedded rigid-damage interface at element side Γ_1^e behaves elastically if the damage activation condition in Eq.(32) is negative at all points of interface $\left(\phi(\boldsymbol{x}) < 0 \text{ for } \boldsymbol{x} \in \Gamma_1^e\right)$. The elastic behaviour of the interface is modelled by the traction separation law in Eq.(29) and the interface compliance matrix in Eq.(22) assumes the following form

$$\mathbf{C}_e^{\Gamma} = \int_{\Gamma_1^e \subset \Gamma_0} \frac{\omega}{1-\omega} \mathbf{S}_e^T \mathbf{n}_1^e \, \mathbf{A}^{el} \mathbf{n}_1^{eT} \mathbf{S}_e d\Gamma = \sum_{g \in \mathcal{G}_1^e} \frac{\omega_g}{1-\omega_g} \mathbf{S}_g^{eT} \mathbf{n}_g^e \, \mathbf{A}^{el} \mathbf{n}_g^{eT} \mathbf{S}_g^e J_g \mathrm{w}_g. \tag{36}$$

where: $\mathcal{G}_1^e$ is the set of integration points $\boldsymbol{x}_g \in \Gamma_1^e$, $\mathbf{S}_g^e = \mathbf{S}_e(\boldsymbol{x}_g)$, $\mathbf{n}_g^e = \mathbf{n}_1^e(\boldsymbol{x}_g)$, $J_g = J(\boldsymbol{x}_g)$ is the Jacobian of isoparametric mapping of element side Γ_1^e and w_g is the integration point weight. The solution of an elastic loading step of an element with embedded rigid-damage interface can be performed using the element Equation (23) with the additional compliance matrix in Eq.(36). Moreover, the undamaged condition of a pristine interface ($\omega_g = 0$ with $g \in \mathcal{G}_1^e$) ensues that the additional compliance matrix is null $\left(\mathbf{C}_e^{\Gamma} = \mathbf{0}\right)$ and, as a clear consequence, a pristine interface can be implicitly considered embedded at every element side and explicitly modelled only when the damage activation condition in Eq.(32) is attained.

3.2 | Damaging loading step

When the damage activation condition is attained, in the pristine interface or in the already partially damaged one, the damage increases and the first of Equations (23), where interfacial elastic compliance matrix is defined in Eq.(36), is not verified. The problem of damage evolution is non-linear and requires an iterative Newton-Rapson (NR) strategy which cannot be solved at the single Gauss point level, as is classically done in displacement based formulation, but it has to be solved for the whole element with the embedded interface and is hereafter described. For a HEE with embedded interface at the loading step $(n+1)$ and for nodal displacement $\mathbf{u}_{(n+1)}^e$ the solution of the incremental damage problem is given by the vector of *generalized stress* $\mathbf{a}_{(n+1)}^e$ and by the vector of damage values $\boldsymbol{\omega}_{(n+1)} = \boldsymbol{\omega}_{(n)} + \Delta\boldsymbol{\omega}$ with $\Delta\omega_g \geq 0$ with $g \in \mathcal{G}_1^e$, which have to verify: the HEE Equation (23), the damage activation condition in Eq.(32) and the flow rules in Eqs.(34- 35). The resolution of such problem has already been faced by the author in Ref.[42], however the formulation proposed in the present paper is significantly improved and simplified. For the sake of simplicity the indexes e and $(n+1)$ are omitted ($\mathbf{u} = \mathbf{u}_{(n+1)}^e$, $\boldsymbol{\omega} = \boldsymbol{\omega}_{(n+1)}$ and $\mathbf{a} = \mathbf{a}_{(n+1)}^e$) and the first of the

Eqs.(23), for a HEE e with the interface embedded at its side Γ_1^e is written in the following residual form

$$\mathbf{R}_e(\omega, \mathbf{a}) = \mathbf{C}_e\mathbf{a} + \int_{\Gamma_1^e} \mathbf{S}_e^T \mathbf{n}_1^e \, \boldsymbol{e}(\omega, \mathbf{a}) \, d\Gamma - \mathbf{H}_e\mathbf{u} = \mathbf{0} \tag{37}$$

where $\boldsymbol{e}(\omega, \mathbf{a}) = \frac{\omega}{1-\omega}\mathbf{A}^{el}\boldsymbol{s}(\mathbf{a})$ is the separation displacement of the interface and the traction $\boldsymbol{s}$ is defined in Eq.(20). The evolution of damage is considered only for that Gauss points $\boldsymbol{x}_g$ where the activation condition is not verified at the beginning of the loading step (iteration $i = 0$ of NR process) and the set of *active* integration points is denoted by $\mathcal{D}_1^e \cup \mathcal{G}_1^e$, that is $\phi_g^{(0)} \equiv \phi\left(\omega_g^{(0)}, \boldsymbol{s}^{(0)}\left(\boldsymbol{x}_g\right)\right) \geq 0$ with $g \in \mathcal{D}_1^e$, while others points are considered as elastic with null damage increments. If one or more integration points results *active*, i.e. with non-negative activation function, at the end of the NR process, than the iterative procedure is repeated including such points.

The damage value $\omega_g^{(i)}$ of an *active point* $g \in \mathcal{D}_1^e$ at iteration (i) of the NR process is updated by enforcing the activation condition in Eq.(32), namely the new value of damage $\omega_g^{(i+1)}$ is obtained by assuming null the damage activation function for a given traction $\boldsymbol{s}_g^{(i)}$, as follows:

$$\phi\left(\omega_g^{(i+1)}, \boldsymbol{s}_g^{(i)}\right) = \frac{1}{\left(1-\omega_g^{(i+1)}\right)^2} \boldsymbol{s}_g^{(i)T} \mathbf{A}^{el} \boldsymbol{s}_g^{(i)} - s_0^2/2k_0 = 0, \tag{38}$$

from which, due to the diagonal form of interface elastic compliance matrix ($A_{ij}^{el} = \delta_{ij}/k_0$), the following updated damage value is obtained

$$\omega_g^{(i+1)} = 1 - \frac{\sqrt{\boldsymbol{s}_g^{(i)T} \boldsymbol{s}_g^{(i)}}}{s_0}. \tag{39}$$

It is noteworthy that the increment of damage $\Delta\omega_g = \omega_g^{(i+1)} - \omega_g$ may be negative, specially at the first iterations, and its positiveness is checked at the end of the iterative process.

The correction of damage modifies also the separation displacement in Eq.(29) which assumes the following updated form

$$\bar{\boldsymbol{e}}_g^{(i)} = \frac{\omega_g^{(i+1)}}{1-\omega_g^{(i+1)}} \mathbf{A}^{el} \boldsymbol{s}_g^{(i)} = \left(\frac{s_0}{\sqrt{\boldsymbol{s}_g^{(i)T} \boldsymbol{s}_g^{(i)}}} - 1 \right) \mathbf{A}^{el} \boldsymbol{s}_g^{(i)} \tag{40}$$

At non *active points* damage and separation displacement are not modified, that is: $\omega_g^{(i+1)} = \omega_g^{(i)}$ and $\bar{\boldsymbol{e}}_g^{(i)} = \boldsymbol{e}_g^{(i)}$.

The iterative process of incremental damage is outlined in the Figures 3a, b where separation displacement and traction at the loading step $(n+1)$ are compared to the theoretical bilinear response, for the partially damaged condition in Fig.3a and for the pristine condition in Fig.3b. In Figures 3a, b the solution at the previous loading step (n) is represented by the traction and the separation displacement $\boldsymbol{e}_{(n)} = \mathbf{A}\left(\omega_{(n)}\right)\boldsymbol{s}_{(n)}$. The trial solution (iteration $i = 0$) at the loading step $(n+1)$ assumes an elastic behaviour with damage $\omega^{(0)} \equiv \omega_{(n+1)}^{(0)} = \omega_{(n)}$ and the elastic response is represented by the separation displacement $\boldsymbol{e}^{(0)} = \mathbf{A}\left(\omega^{(0)}\right)\boldsymbol{s}^{(0)}$ and traction $\boldsymbol{s}^{(0)}$, which does not verify the damage activation condition, that is $\phi = Y\left(\omega^{(0)}, \boldsymbol{s}^{(0)}\right) - Y_0 > 0$. The consequent damage correction given in Eq.(39) modifies the separation displacement to the new value $\bar{\boldsymbol{e}}^{(0)} = \frac{\omega^{(1)}}{1-\omega^{(1)}}\mathbf{A}^{el}\boldsymbol{s}^{(0)}$ which clearly shows the negative damage increment at the first iteration in both the partially damage condition and in the pristine one. In particular, in the pristine state the activation condition is attained with null separation displacement and the negative value of the modified separation displacement $\bar{\boldsymbol{e}}^{(0)}$ with positive traction, is due to a negative value of damage at the first correction.

It can be observed that updated values of damage and of separation displacement only depend on traction at the current iteration ($\boldsymbol{s}_g^{(i)}$), which is function of *generalized stress* vector $\mathbf{a}^{(i)}$ (see Eq.(20)). As a consequence, residual in Eq.(37) can be likewise written as function of the *generalized stress* vector, that is

$$\bar{\mathbf{R}}_e\left(\mathbf{a}^{(i)}\right) = \mathbf{R}_e\left(\omega^{(i+1)}, \mathbf{a}^{(i)}\right) = \mathbf{C}_e\mathbf{a}^{(i)} + \int_{\Gamma_1^e} \mathbf{S}_e^T \mathbf{n}_1^e \, \bar{\boldsymbol{e}}^{(i)}. \, d\Gamma - \mathbf{H}_e\mathbf{u} \neq \mathbf{0} \tag{41}$$

The solution of Eq.(37) can be approached by an iterative NR method by the following approximation of the residual in a Taylor expansion limited to the first term, that is

$$\bar{\mathbf{R}}_e\left(\mathbf{a}^{(i+1)}\right) \approx \bar{\mathbf{R}}_e\left(\mathbf{a}^{(i)}\right) + \frac{d\bar{\mathbf{R}}_e}{d\mathbf{a}}\Delta\mathbf{a} = \mathbf{0}. \tag{42}$$

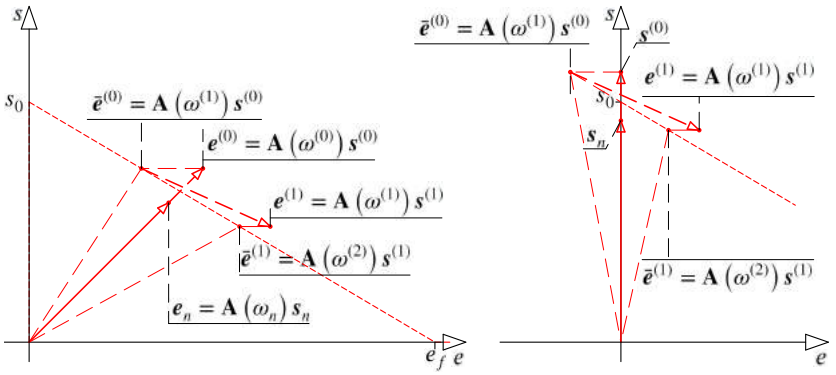

FIGURE 3 Correction of traction and separation displacement in the iterative process of incremental damage are compared to the theoretical bilinear response for: a) partially damaged interface; b) pristine interface. The solution at the previous loading step (n) is represented by separation displacement $\boldsymbol{e}_{(n)} = \mathbf{A}\left(\omega_{(n)}\right)\boldsymbol{s}_{(n)}$. The trial solution (iteration $i = 0$) at the loading step $(n+1)$ is $\boldsymbol{e}^{(0)} = \mathbf{A}\left(\omega^{(0)}\right)\boldsymbol{s}^{(0)}$. Separation displacement after damage correction is $\bar{\boldsymbol{e}}^{(0)} = \frac{\omega^{(1)}}{1-\omega^{(1)}}\mathbf{A}^{el}\boldsymbol{s}^{(0)}$.

In detail, the total derivative of the residual is defined as follows

$$\frac{d\bar{\mathbf{R}}_e}{d\mathbf{a}} = \mathbf{C}_e + \mathbf{C}_e^{\Gamma} + \mathbf{C}_e^{\Gamma cs} \tag{43}$$

where

$$\mathbf{C}_e^{\Gamma cs} = \int_{\Gamma_1^e} \mathbf{S}_e^T \mathbf{n}_1^e \, \mathbf{A}^{cs} \, \mathbf{n}_1^{eT} \mathbf{S}_e \, d\Gamma = \sum_{g \in \mathcal{D}_1^e} \mathbf{S}_g^{eT} \mathbf{n}_g^e \, \mathbf{A}_g^{cs} \mathbf{n}_g^{eT} \mathbf{S}_g^e J_g w_g. \tag{44}$$

is the consistent compliance matrix of the interface due to the damage evolution and the following matrix

$$\mathbf{A}_g^{cs} = -\frac{s_0}{k_0 \left(\boldsymbol{s}_g^{(i)T} \boldsymbol{s}_g^{(i)}\right)^{\frac{3}{2}}} \boldsymbol{s}_g^{(i)} \otimes \boldsymbol{s}_g^{(i)} \tag{45}$$

models the constitutive non-linear behaviour with incremental damage of *active* integration points $g \in \mathcal{D}_1^e$. The *generalized stress* can be iteratively corrected as follows

$$\mathbf{a}^{(i+1)} = \mathbf{a}^{(i)} + \Delta\mathbf{a} = \mathbf{a}^{(i)} - \left[\mathbf{C}_e + \mathbf{C}_e^{\Gamma} + \mathbf{C}_e^{\Gamma cs}\right]^{-1} \bar{\mathbf{R}}_e\left(\mathbf{a}^{(i)}\right) \tag{46}$$

and the NR process converges in few iterations and stops when the relative error of the damage activation condition respect to its initial value, in all the active Gauss points, is lower than a fixed tolerance t_ω, that is: $\left|\phi\left(\omega_g^{(i)}, \boldsymbol{s}_g^{(i)}\right)\right| \leq t_\omega \phi_g^{(0)}$ with $g \in \mathcal{D}_1^e$.

3.3 | Full debonding condition

The full debonding condition with null traction at the interface and damage $\omega = 1$ produces a null stiffness matrix and its implementation is a trivial problem in displacement-based formulation. Conversly, such a problem cannot be analysed in HEE formulation by same the approach proposed in the previous section, for which the interface compliance matrix defined in Eq.(36) assumes an indeterminate form at the fully debonded points.

The problem of full debonding condition has already been addressed by the author in Ref.[42] by a Lagrangian approach which is hereafter described. The set of fully damaged integration points at the embedded interface Γ_1^e is denoted by $\mathcal{L}_1^e$, that is: $\omega_l = 1$ at points $\boldsymbol{x}_l \in \Gamma_1^e$ with $l \in \mathcal{L}_1^e$. The interface compliance matrix is evaluated only at pristine or partially damaged integration points and is defined as follows

$$\mathbf{C}_e^{\Gamma} = \sum_{g \in \mathcal{G}_1^e - \mathcal{L}_1^e} \frac{\omega_g}{1-\omega_g} \mathbf{S}_g^{eT} \mathbf{n}_g^e \, \mathbf{A}^{el} \mathbf{n}_g^{eT} \mathbf{S}_g^e J_g \mathrm{w}_g. \tag{47}$$

and the equation of a HEE with one or more fully damaged integration points at the embedded interface Γ_1^e assumes the following form

$$\begin{bmatrix} \mathbf{C}_e + \mathbf{C}_e^{\Gamma}(\omega) & \mathbf{L}_e & -\mathbf{H}_e \\ \mathbf{L}_e^T & \mathbf{0} & \mathbf{0} \\ -\mathbf{H}_e^T & \mathbf{0} & \mathbf{0} \end{bmatrix} \begin{bmatrix} \mathbf{a}_e \\ \boldsymbol{\delta}_e \\ \mathbf{u}_e \end{bmatrix} = \begin{bmatrix} \mathbf{0} \\ \mathbf{0} \\ -\mathbf{q}_e \end{bmatrix}. \tag{48}$$

where $\mathbf{L}_e = \left\{ \mathbf{S}_l^T \mathbf{n}_l^e \text{ with } l \in \mathcal{L}_1^e \right\}$, $\boldsymbol{\delta}_e = \left\{ \boldsymbol{\delta}_l \text{ with } l \in \mathcal{L}_1^e \right\}$ is a vector collecting the Lagrangian variables, each of which measures the separation displacements $\boldsymbol{\delta}_l = \boldsymbol{e}\left(\boldsymbol{x}_l\right)$ at fully damaged integration points, and the second row of Eq.(48) gives the condition of null traction, that is: $\mathbf{n}_l^{eT} \mathbf{S}_l^e \mathbf{a}_e = \boldsymbol{s}\left(\boldsymbol{x}_l\right) = \mathbf{0}$ with $l \in \mathcal{L}_1^e$.

The Lagrangian approach is employed both for the linear elastic loading step and for the non-linear one with increasing damage (for more details see Ref.[42]).

4 | COHESIVE CRACK GROWTH

The HEE formulation with embedded interface at the element side can model elements with curved sides. However, all the internal sides Γ_s with $s \in \mathcal{B}_{int}$ are modelled as straight sides and only the element sides Γ_s with $s \in \mathcal{B}_T \cup \mathcal{B}_U$ at the external boundary are allowed to be curved. Only one extrinsic interface can be embedded per element and, in a two-dimensional problem, the crack can be spatially modelled by a piece-wise linear geometry. Moreover, the crack branching can also be modelled.

The HEE formulation is coupled with the embedded extrinsic interface to simulate inter-element crack propagation in quasi-brittle materials. The same problem has been as already approached by the Author in Ref.[42] by a formulation with fixed mesh and with a mixed mode crack opening condition, with the consequent mesh dependence of the crack trajectory and of the overall response. In Ref.[42] the crack propagations condition coincides to the damage activation condition in Eq.(32), which is governed both by the tensile traction component and by the tangential one.

In the present paper, the criterion assumed for determining the growth direction is that of the maximum principal stress[14], which is, in author's opinion, the most suitable criterion for the analysis of cohesive crack propagation in isotropic quasi-brittle materials by the stress based approach proposed in the manuscript. Other relevant criteria for determining the direction of crack growth are the maximum energy release rate criterion[57] and the minimum strain energy density criterion[58], but they can be considered more suitable in an elastic fracture based framework. Based on the maximum principal stress criterion, crack grows when the maximum principal stress σ_1 (with principal direction $\boldsymbol{n}_1$) reaches the tensile strength value s_0 and the crack propagates in the orthogonal direction $\boldsymbol{n}_2 \perp \boldsymbol{n}_1$, which generally does not coincides to any element edge. Therefore the mesh around crack tip must be adapted to the direction $\boldsymbol{n}_2$, by rotation of the element sides, so that the embedded interface is aligned to the crack growth direction $\boldsymbol{n}_2$.

4.1 | Crack propagation and local re-meshing

The crack growth criterion is checked at the three vertexes of all pristine elements at the end of each loading step, once reached the convergence of the non-linear steps. The crack propagates as an inter-element interface embedded at an element edge when the maximum principal stress at one of the three element vertexes reaches the tensile strength ($\sigma_1 \geq s_0$) and the direction of propagation $\boldsymbol{n}_2$, which is orthogonal to the maximum stress direction $\boldsymbol{n}_1$, crosses the element or coincides to one of the two straight sides of the vertex. The vertex where crack growth criterion is verified is called *active vertex* and coincides to the crack tip of the existing embedded crack when crack propagates. The HEE where the crack propagates is called *Crack Propagation Element* (CPE). If direction of propagation $\boldsymbol{n}_2$ coincides to one the two straight sides of the *active vertex* the inter-element crack is embedded at this side of the CPE without any remeshing. Whereas, in the most general case direction of propagation $\boldsymbol{n}_2$ crosses the CPE and the mesh surrounding this element has to be adapted to direction $\boldsymbol{n}_2$. In detail, the straight side closest to direction of propagation $\boldsymbol{n}_2$ rotates around the *active vertex* and the inter-element crack is embedded at this side.

The problem of crack propagation from element e_0 to element e_1 is represented in Fig.4a, where the mesh surrounding crack tip is represented with the existing crack embedded in element e_0 at its side $\Gamma_1^{e_0}$. The mesh is composed of nine-node elements and the crack growth criterion is checked in all the pristine elements. In element e_1 the principal stresses $\sigma_1 > \sigma_2$ at the crack tip (geometrically coincident to nodes 3 and 4) are represented in the Figure with the relevant directions $\boldsymbol{n}_1 \perp \boldsymbol{n}_2$. Element e_1 is the *Crack Propagation Element* and the *active vertex* coincides to nodes 3 and 4. The propagation criterion is verified with $\sigma_1 \geq s_0$ and the direction of crack propagation $\boldsymbol{n}_2$ is internal to the element e_1, so remeshing of elements surrounding crack tip has to be performed in order to have the closest element side ($\Gamma_1^{e_1}$ in Fig.4a) aligned to the direction of crack propagation $\boldsymbol{n}_2$.

The remeshing procedure involves also the adjacent elements which share nodes 1 and 9 of element e_1 or which have nodes geometrically coincident to these nodes. In order to have a modified mesh with similar sizes of the two adjacent element elements e_1 and e_2, remeshing is performed by moving the second end of the element side $\Gamma_1^{e_1}$ (nodes 1 and 9) to the intersection between crack propagation direction $\boldsymbol{n}_2$ and the orthogonal to the segment connecting the corners of elements e_1 and e_2 opposite to the common side.

In Fig.4b the same part of the mesh is depicted after the minimal re-meshing. The side $\Gamma_1^{e_1}$ of element e_1 is rotated around the *active vertex* so that to the straight side $\Gamma_1^{e_1}$ is coincident to the direction of propagation ($\boldsymbol{t}_1^{e_1} \parallel \boldsymbol{n}_2$). Translation of nodes at the second end of side $\Gamma_1^{e_1}$, due to the mesh adaptation, is represented in Fig.4a by means of by vector $\boldsymbol{v}$; translations of mid side nodes keep the side straight and preserve their relative position at the side, *e.g.* the mid-side nodes of the nine-node elements moves to the mid-side position of the new straight side. The new section of the crack is embedded into side $\Gamma_1^{e_1}$ of element e_1.

Remark. For each *active* HEE, the direction of propagation of the embedded crack is fixed at its activation and it does not modify even if the principal stress directions $\boldsymbol{n}_1$ and $\boldsymbol{n}_2$ at the *active vertex* change.

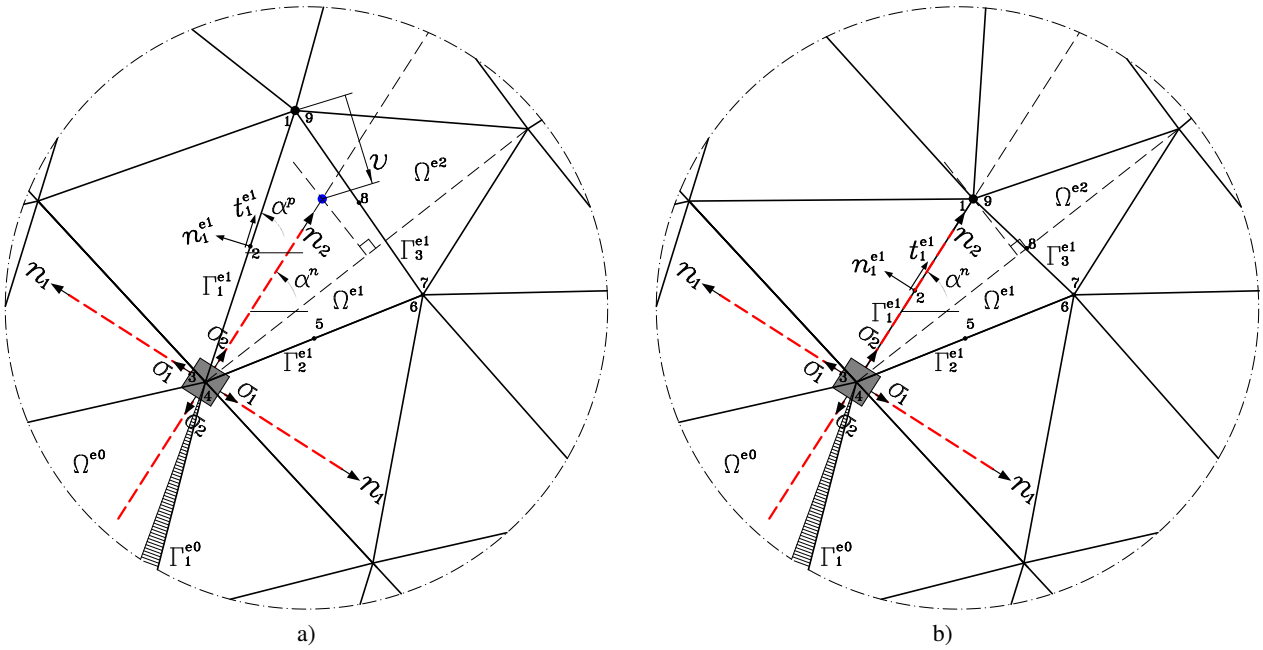

FIGURE 4 Crack propagation from element e_0 to element e_1. a) The interface is embedded at side $\Gamma_1^{e_0}$ of element e_0. The maximum principal stress criterion is verified at a vertex of element e_1 with $\sigma_1 \geq s_0$ and with direction of crack propagation $\boldsymbol{n}_2$ internal to the element. b) The side $\Gamma_1^{e_1}$ of element e_1 is rotated around the vertex so that to the straight side $\Gamma_1^{e_1}$ is coincident to the direction of propagation ($\boldsymbol{t}_1^{e_1} \parallel \boldsymbol{n}_2$).

4.2 | Modified crack propagation criterion

A deep numerical investigation of cohesive crack problems shows that the criterion of crack propagation described in the previous Section models the correct direction of crack propagation, compared to experimental data, only at the beginning of the cracking process and tends progressively to fail as long as the process zone width increases. The reasons of such erroneous evaluation of the direction of crack propagation are hereafter analysed.

At the first formation of crack the width of process zone is practically null and the cracking phenomena can be regarded as a fracture mechanics problem. Moreover, neglecting the problem of stress singularity at the crack tip, which cannot be caught through the proposed formulation, the state of stress at the activation condition almost coincides to pure mode I debonding

condition, with $\sigma_1 = s_0$ and $\sigma_2 \approx 0$. Under such a condition the principal directions of stress and the direction of crack propagation are univocally defined. As long as the applied load increases and the process zone extends, the first principal stress at the crack tip remains limited to the strength values, *i.e.* $\sigma_1 \leq s_0$, while the second principal stress increases and the two-dimensional stress state tends to became hydrostatic with $\sigma_1 \approx \sigma_2 \leq s_0$ with uncertain and numerically unstable direction of crack propagation. Furthermore, in a fully cohesive crack propagation and with the limitation of the first principal stress to the strength value ($\sigma_1 \leq s_0$) the inversion of principal stresses, with $\sigma_2 \geq \sigma_1 \geq s_0$, can also be observed with the consequent rotation of the new crack direction of an angle $\pm\pi/2$ with respect the previous section of crack.

The directional bias of crack propagation is well known in literature [59,60] and several resolution strategies have been proposed. In Ref.[61] a mesh-induced erroneous direction of propagation was encountered with both pure embedded crack and coupled smeared-embedded crack. The numerical difficulties were mitigated by a non-local formulation of the smeared part of the model. In Ref.[62] the crack was embedded in a C^1 continuity displacement based formulation, which employs Powell-Sabin B-splines and produces smooth stress field around the crack tip. The criterion for crack nucleation was initially based on such smooth stress field, giving a directional bias of crack propagation, but was improved by an the use of an averaged stress tensor.

In order to overcome such a numerical instability, the following modified crack propagation criterion is proposed: the angle α^w (from the x-axis) of the direction of crack propagation $\bar{\boldsymbol{n}}_2$ is given as *weighted* mean value between the angle α^p of the previous section of crack and the angle α^n of principal direction $\boldsymbol{n}_2$ at the *active vertex*; that is

$$\alpha^w = (1-r)\alpha^p + r\alpha^n \tag{49}$$

$$r = \frac{|\sigma_1 - \sigma_2|}{\sigma_1 + \sigma_2} = \frac{\tau_{max}}{\sigma_m} \tag{50}$$

where the weighting parameter r is the stress ratio between the maximum tangential stress τ_{max}, or the radius of the Mohr circle of the two-dimensional stress state, and the mean stress σ_m that is the coordinate of the centre of the Mohr circle. The three angle α^w, α^p and α^n are represented in Fig. 5 for a parameter $r = 0.5$.

The proposed parameter properly governs the transition from the initial cracking process, with pure mode I stress state, to the fully cohesive crack propagation with, in case, hydrostatic stress state. At the initial cracking process, with pure mode I stress state, the weighting parameter is $r = 1$ and the angle of crack propagation coincides to the angle of principal direction $\bar{\boldsymbol{n}}_2 \equiv \boldsymbol{n}_2$ (or $\alpha^w = \alpha^n$) at the *active vertex* of the element crossed by the new section of crack. On the contrary, in a fully cohesive crack propagation with almost hydrostatic stress state the weighting parameter is $r = 0$ and the crack grows with the same angle of the previous section of crack ($\alpha^w = \alpha^p$).

In a fully cohesive crack propagation regime, the inversion of the principal stresses can also produce branching with activation of crack orthogonal to the second principal stress σ_2 and the modified criterion assumes a direction of crack $\bar{\boldsymbol{n}}_1$ with the following *weighted* angle $\beta^w = (1-r)\beta^p + r\beta^n$, where: $\beta^p = \alpha^p \pm \pi/2$ is the angle of the direction orthogonal to the previous section of crack and $\beta^n \approx \alpha^n \pm \pi/2$ is the angle of principal direction $\boldsymbol{n}_1$. It is noteworthy that the two directions of propagation $\bar{\boldsymbol{n}}_1$ and $\bar{\boldsymbol{n}}_2$ are generally not perfectly orthogonal, as the principal direction $\boldsymbol{n}_1$ and $\boldsymbol{n}_2$ refers to *active vertexes* geometrically coincident but of different elements, so with different stress states.

The modified crack propagation criterion applied to crack growing and to crack branching is represented in Figs.5 where the crack grows from element e_0 to element e_1 and also branches to element e_2. In Fig.5 the mesh surrounding crack tip is represented and the inter-element crack is embedded within element e_0 at its side $\Gamma_1^{e_0}$. The maximum principal stress criteria is verified in element e_1 with $\sigma_1 \geq s_0$ and in element e_2 with $\sigma_2 \geq s_0$. For sake of simplicity, the same principal directions $\boldsymbol{n}_1$ and $\boldsymbol{n}_2$ are represented at the vertex of element e_1 and at the vertex of element e_2, but the stress fields of the elements, and the relevant principal directions, are one independent of each other. In the figure, directions of propagation $\bar{\boldsymbol{n}}_2$ of angle α_w crosses element e_1 and directions of branching $\bar{\boldsymbol{n}}_1$ of angle β^w crosses element e_2, so the mesh surrounding these elements has to be adapted by rotation of the straight sides closest to the directions of propagation around the relevant *active vertexes* and inter-element cracks have to be embedded at these sides. Remeshing is represented in Fig.5 by the vectors v_1 and v_2, which show the translation applied to the vertex nodes.

The proposed criterion of cohesive crack propagation can model a progressive variation of crack direction, in case, with transversal crack, but it cannot model an abrupt change in the direction of crack. In order to avoid spurious oscillation of crack direction, a maximum value $\Delta\alpha_{max}$ of rotation angle between two consecutive branches of crack is established, which can be summarized by the following relations: $|\alpha^w - \alpha^p| \leq \Delta\alpha_{max}$ and $|\beta^w - \beta^p| \leq \Delta\alpha_{max}$.

The proposed remeshing procedure can lead to the formation of elements with bad-aspect ratio, which *per se* does not induce instability or pathological response. In fact, the formulation is not based on an isoparametric mapping and stress fields are defined

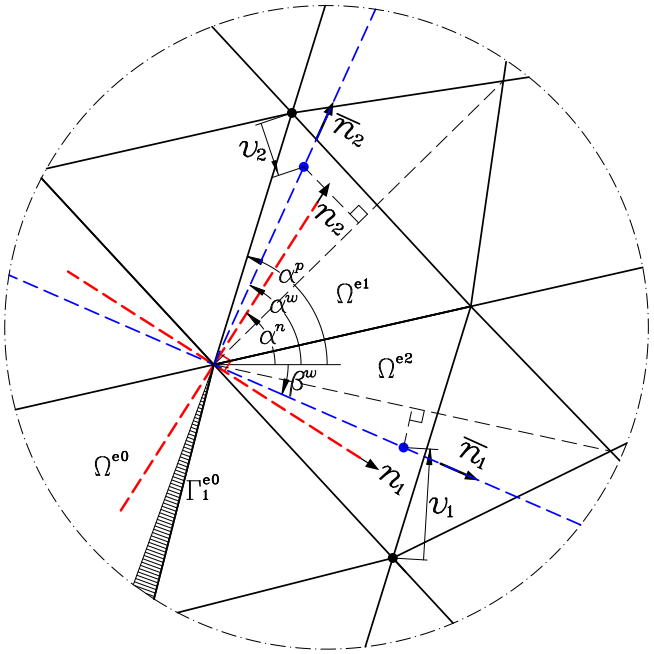

FIGURE 5 Representation of crack propagation, from element e_0 to elements e_1 and representation of crack branching, from element e_0 to elements e_2. The principal stress criterion is verified at the *active vertexes* of element e_1 with $\sigma_1 \geq s_0$ with modified direction of crack propagation $\bar{\boldsymbol{n}}_2$, of angle α^w, internal to the element; the relevant remeshing is governed by the translation vector $\boldsymbol{v}_2$. The criterion also is verified at the *active vertexes* of element e_2 with $\sigma_2 \geq s_0$ and with direction of crack branching $\bar{\boldsymbol{n}}_1$, of angle β^w, internal to the element; the relevant remeshing is governed by the translation vector $\boldsymbol{v}_1$.

directly in Cartesian coordinates and, although with bad aspect ratio, a HEE gives a solution which strongly satisfies equilibrium equations. Nevertheless, this problem has been addressed locally for an element with angle corner $\alpha > \frac{2}{3}\pi$ and for the adjacent element that shares the side opposite to such corner, as represented in Fig.6a. The elements e_1 and e_2 form a quadrilateral where the common side is a diagonal. The remeshing procedure modifies the two elements changing the common side to the second diagonal of the quadrilateral, as represented in Fig.6b.

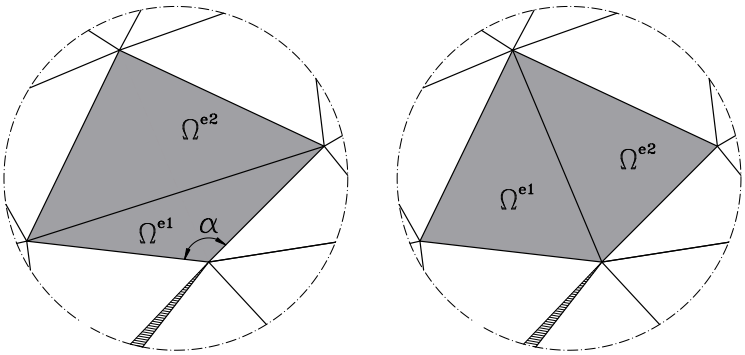

FIGURE 6 Representation of remeshing procedure for elements with angle corner $\alpha > \frac{2}{3}\pi$.

5 | NUMERICAL SIMULATION

The HEE formulations has been implemented in the finite element code FEAP v8.5 [63] using a triangular HEE with the quadratic, cubic and quartic stress fields. In detail, the nine-node hybrid equilibrium element (HEE2) with the quadratic stress field, the twelve-node element (HEE3) with the cubic stress field and the fifteen-node element (HEE4) with quartic stress field are represented in Figs.1a, c. The accurate performances of the purely elastic formulation with high-order stress fields, for both the analysis of static and dynamic problems, have been investigated by the author in Refs. [42,49].

The HEE formulation with triangular two-dimensional elements can be affected by Spurious Kinematic Modes on well-known patches of elements, as described in Refs. [51,52,64,65,66]. These SKMs can be restrained by the approach proposed in Ref. [51]. However, the numerical simulations proposed in this paper are based on meshes which are not affected by any SKM. The mesh generator creates hexagonal geometry of triangular HEE, in a honeycomb-like pattern, with at least three elements at the boundary edges and two elements at the corners. Therefore, no one of the three SKMs (single element at a corner, two elements at a straight boundary edge and four internal elements forming a closed star with diagonal internal sides) analysed in Ref. [51] are modelled in the mesh.

5.1 | Three points bending test

The first numerical simulation is the three point bending test (3PBT) of a symmetric beam with a pre-existing crack at the notch. Set-up and dimensions of the 3PBT with relevant boundary conditions are represented in Fig. 7 a. Only the area of the two-dimensional domain between the two lower support points, which is highlighted in grey in the Figure, is discretized in the numerical simulation. The loading test is numerically modelled under displacement control, so the load is applied by imposed vertical displacement at the upper edge midpoint and the history of the resultant force at the loading point is captured. The 3PBT of symmetric beam with single edge cracked is well known in literature [67,68,69] and, for the present paper, the numerical simulation was performed with the same dimensions and with the same material parameters of the concrete beam proposed in Ref. [67]. The material parameters are: Young's modulus $E = 20\,\text{GPa}$; Poisson's ratio $\nu = 0.2$; tensile strength $s_0 = 2.5\,\text{MPa}$; fracture energy $G_I = 0.1\,\text{N mm}^{-1}$.

Due to the symmetry of analysed problem, and as already shown in Refs. [67,68,69], the crack has to propagate along the vertical line between the tip of existing crack and the loading point at the upper edge. In order to test validity and effectiveness of the proposed formulation the 3PBT is modelled by two different meshes, which are plotted in Figs. 7b, c. The Mesh 1 plotted in Fig.7b is defined by HEEs with vertical sides so that the vertical line where the crack has to propagate is already modelled. Conversely, Mesh 2 plotted in Fig.7c has horizontal element sides and the vertical line of the crack is not discretized. Therefore, in order to model the vertical crack, the element sides at the crack tip has to be rotated according to the re-meshing approach proposed in Sec.4. The numerical results of the TPBT were carried with quadratic stress field and nine-node HEEs.

The numerical responses of the single edge cracked 3PBT, carried out by the two meshes, are plotted in Fig. 8 in terms of imposed displacement u and reaction force F and are compared to the theoretical maximum carrying load, which was calculated using the theory of Linear Elastic Fracture Mechanics (LEFM) in Ref. [67]. The labels a and b in the Figure respectively point out the loading conditions corresponding to vertical displacements $u_a = 0.14\,\text{mm}$ and $u_b = 0.28\,\text{mm}$, to which the following stress maps have been carried out. The colour contour maps of the maximum principal stress at the two considered loading conditions , obtained by finite element simulation with HEE and embedded interface for Mesh 1 of Fig.7b, are respectively plotted in Figs.9a and b. These maps of stress are plotted in the deformed configuration showing a perfectly symmetric response with a correct propagation of a vertical crack. Moreover, it can be observed in Fig.9b that, due to the inversion of the principal directions at the crack tip, the element sides have been rotated along the horizontal direction, which is orthogonal to the direction of crack. The rotated sides undergo an initial damage activation at the Gauss point geometrically coincident to the crack tip, but crack propagates only in vertical direction. Figure 9a shows that such phenomenon is not observed at the beginning at the cracking process. The colour contour maps of the maximum principal stress at the same loading conditions of vertical displacements $u_a = 0.14\,\text{mm}$ and $u_b = 0.28\,\text{mm}$ (labels a and b in Fig.8) and achieved by Mesh 2 plotted in Fig.7c, which does not model the vertical sides, are respectively plotted in Figs.10a and b. There can be observed that the crack carried out in the numerical simulation is still vertical, but the solution is not perfectly symmetric. In fact, the rotation of the element sides along the vertical direction generates an nonsymmetric mesh, which cannot produce a symmetric response. The comparison of the responses obtained with the two different meshes shows an overall very good agreement.

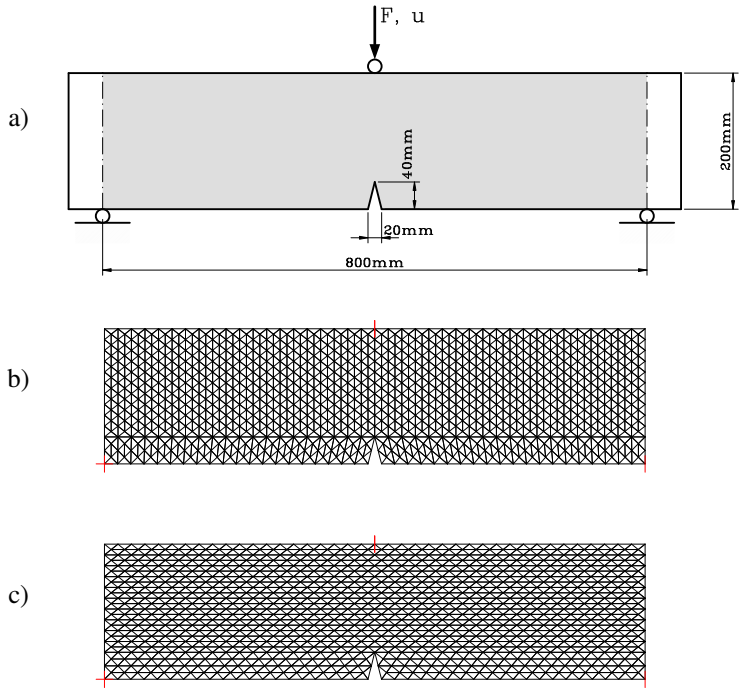

FIGURE 7 Single edge cracked 3PBT of beam with pre-existing crack: a) set-up and dimensions; b) mesh 1, with vertical element sides; c) mesh 2, with horizontal element sides.

5.2 | L-shaped concrete panel

The second numerical simulation regards the propagation of a crack into the so called L-shaped concrete panel (LSCP), whose set-up, sizes and boundary conditions are represented in Fig. 11 a. The area of crack experimentally observed is highlighted in dark grey. Thickness of specimen is $t = 100\,\text{mm}$. Experimental results are documented in Ref.[70] and the cracking problem has been numerically modelled through numerous different formulations: in Ref.[69] by a nonlocal peridynamic formulation; in Ref.[71] in a smeared crack approach coupled with a tensile stress damage; in Ref.[72] the numerical results of a strong discontinuity approach are compared to the results obtained with a fracture energy based smeared crack formulation.

The numerical simulation was performed under displacement control, therefore load was applied in terms of prescribed vertical displacement and the reaction force at the loading point computed. The material constitutive parameters are: Young's modulus $E = 20\,\text{GPa}$; Poisson's ratio $\nu = 0.18$; tensile strength $s_0 = 2\,\text{MPa}$; fracture energy $G_I = 0.09\,\text{N mm}^{-1}$. This constitutive parameters are slightly different from the experimental ones: $E = 25.85\,\text{GPa}$; $\nu = 0.18$; $s_0 = 2.7\,\text{MPa}$; $G_I = 0.065\,\text{N mm}^{-1}$.

The numerical results were carried with quadratic stress field (HEE2), cubic stress field (HEE3) and quartic stress field (HEE4) with the mesh plotted in Fig.11 b, for which domain was discretized in 1872 quadratic elements and 8571 nodes, in 1872 cubic elements and 11428 nodes and in 1872 quartic elements and 14285 nodes. Moreover, the numerical simulation was performed with the finer mesh plotted Fig.11c with 4400 quadratic elements and 19065 nodes.

The responses of the four numerical analyses carried out for the LSCP are plotted in Fig.12 in terms of imposed displacement u and reaction force F and are compared to the experimental data reported in Ref.[70]. The lower values of the post peak load in the numerical prediction, respect to the experimental load, could be due to aggregate interlock, which could be approached by an elastic-plastic-damage model. A more accurate response could also be modelled with a richer damage softening curve, such as a bilinear one. The labels a and b in this figure respectively point out the condition of maximum load and the solution at vertical displacements $u = 0.4\,\text{mm}$. The colour contour maps of the maximum principal stress, at the loading conditions a and b reported in the graph in Fig.12, given as results of the finite element simulation with quadratic elements (HEE2) and with Mesh 1, are respectively plotted in Figs.13a and b. The colour contour of the maximum principal stress carried out with quadratic elements and with Mesh 2 are respectively plotted in Figs.13c and d. These stress maps are plotted in the deformed configuration and they show almost coincident results, both in terms of stress and in terms of crack path. Moreover, it is noteworthy that the

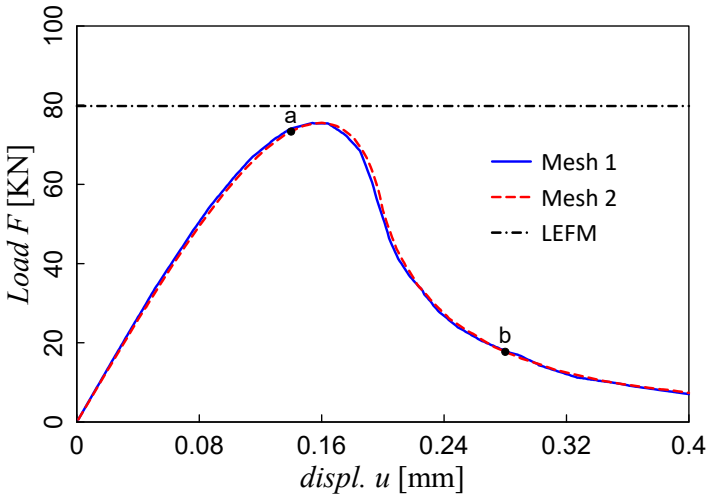

FIGURE 8 Numerical responses of the single edge cracked 3PBT with the meshes plotted in Figs. 8a, b, in terms of imposed displacement u and reaction force F. The numerical results are compared to the theoretical maximum carrying load, calculated by the theoretic formulation of Linear Elastic Fracture Mechanics (LEFM) in Ref.[67]. The labels a and b point out the loading conditions corresponding to vertical displacements $u = 0.14$ mm and $u = 0.28$ mm.

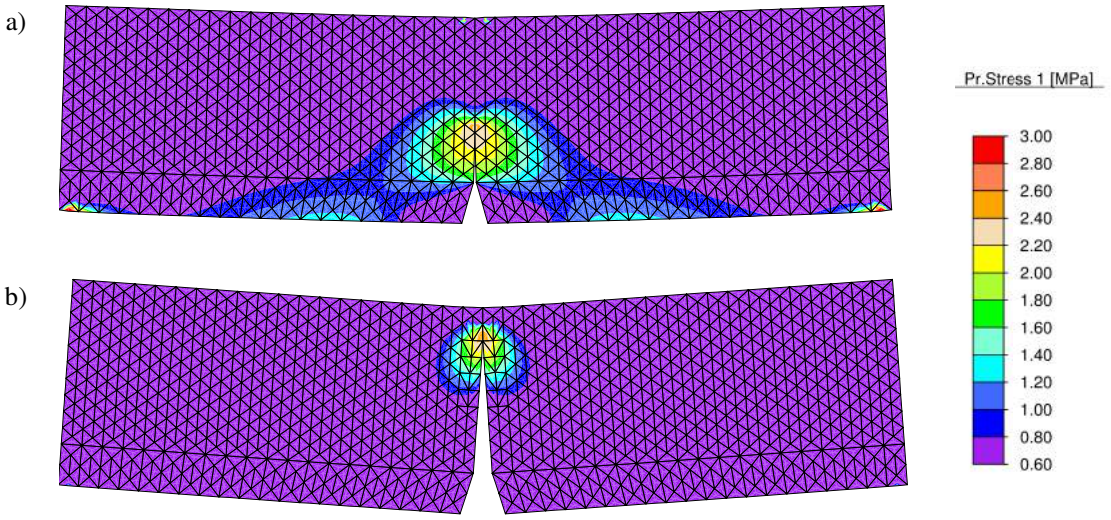

FIGURE 9 Contour of the maximum principal stress carried out by the numerical simulation of the 3PBT with the mesh with vertical sides in Fig.7b, at two loading conditions: a) vertical displacement $u = 0.14$ mm; b) vertical displacement $u = 0.28$ mm

crack paths represented in these figures overlap area of crack experimentally observed and highlighted in Fig.11a. The results of this test show also a remarkable low influence of the element size.

5.3 | Single-edge notched concrete beam

The third numerical simulation regards the propagation of a crack into the Single-Edge Notched concrete Beam (SENB), whose set-up, sizes and boundary conditions are represented in Fig.14, whereas the results of the experimental tests are given in Ref.[73].

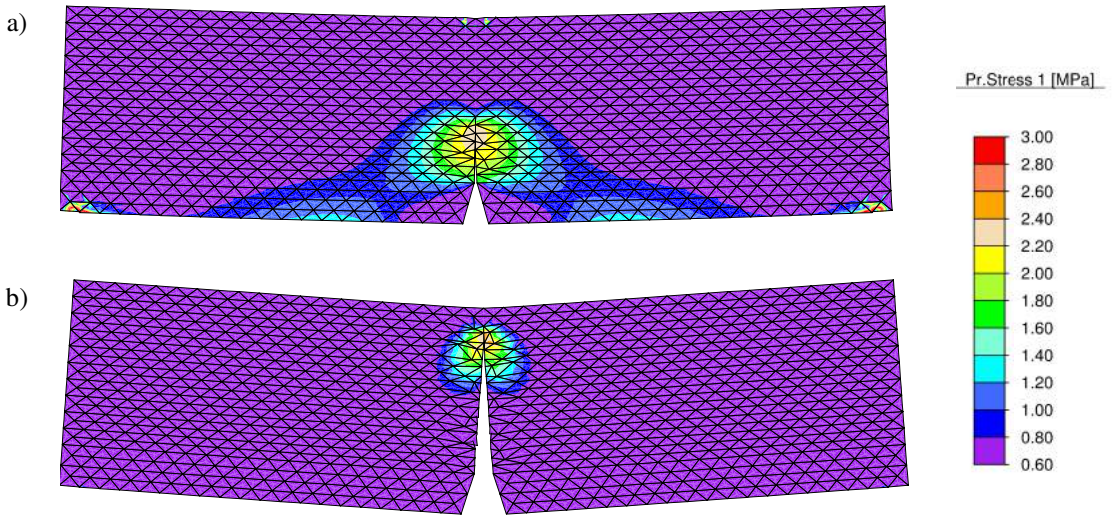

FIGURE 10 Contour of the maximum principal stress carried out by the numerical simulation of the 3PBT with the mesh without vertical sides in Fig.7c, at two loading conditions: a) vertical displacement $u = 0.14$ mm; b) vertical displacement $u = 0.28$ mm

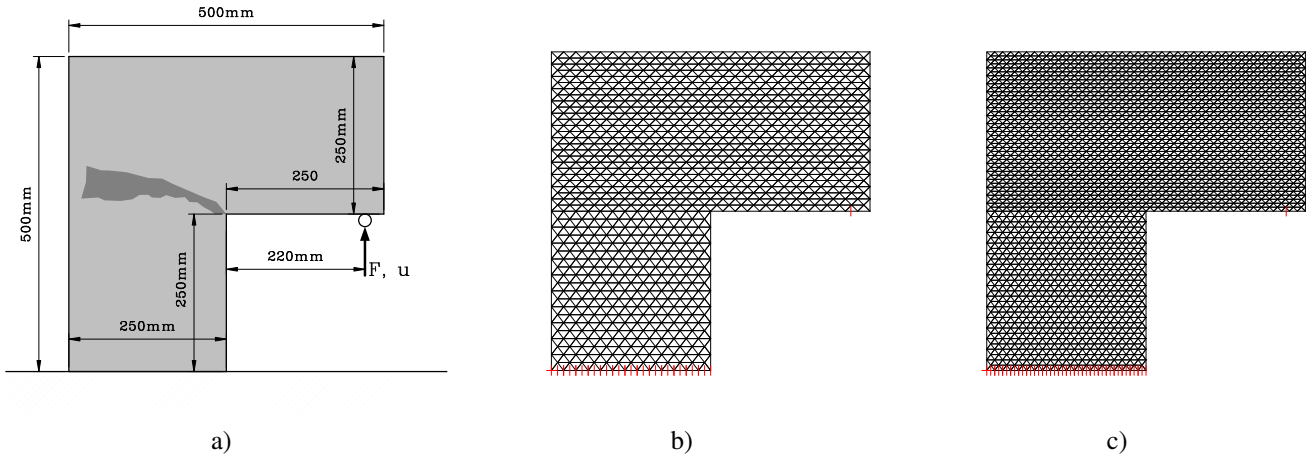

FIGURE 11 a) Set-up and sizes of the L-shaped concrete panel. The zone in dark grey highlights the region where crack is experimentally observed[70]. Thickness is $t = 100$ mm. b) Mesh 1. c) Mesh 2.

The area zone where crack experimentally develops is highlighted in dark grey. Thickness of specimen is $t = 50$ mm and the constitutive parameters are: Young's modulus $E = 38$ GPa; Poisson's ratio $\nu = 0.18$; tensile strength $s_0 = 3$ MPa; fracture energy $G_I = 0.069\,\mathrm{N\,mm^{-1}}$. The left hand side of the concrete beam is irrelevant from the mechanical point of view, being subjected to neither loads nor boundaries, and it is neglected in the domain discretization. The area of the concrete beam discretized in HEE is coloured in light grey in Fig. 14.

The SENB fracture problem was analysed in Ref.[54] in a discontinuous Galerkin finite element formulation (DGM) coupled with rigid-cohesive interface modelled at all the inter-element sides, in Ref.[74] by XFEM approach and in Ref.[69] through a nonlocal peridynamic approach.

The numerical simulation was performed under plane stress conditions with quadratic stress field (HEE2) and the load level was governed by the *arclength* control of the crack opening displacement (CMOD). Two meshes were employed: a coarse one with 2720 elements and 12432 nodes; a finer mesh with 5640 elements and 25656 node.

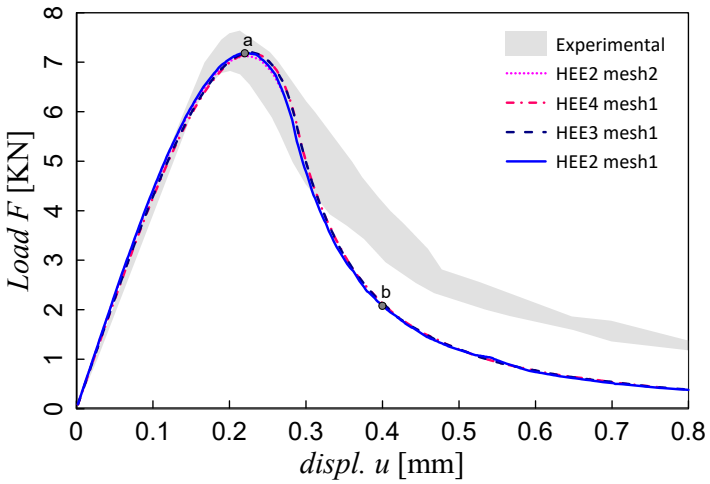

FIGURE 12 Numerical responses of the LSCP, in terms of imposed displacement u and reaction force F. The numerical results are compared to the experimental data reported in Ref. [70]. The labels a and b point out respectively the maximum load conditions and the loading condition corresponding to vertical displacement $u = 0.4$ mm.

The responses of the numerical analyses of SENB carried out with the two meshes are plotted in Fig.15 in terms of CMOD and force F. The numerical results are compared to the experimental data reported in Ref. [73] and to others numerical solutions [54,74,69]. The labels a and b point out respectively the maximum load conditions and the loading condition corresponding to CMOD value of 0.15 mm.

The colour contour maps of maximum principal stress, at the loading conditions a and b reported in the graph of Fig.15, given as results of the finite element simulation with quadratic elements (HEE2) with Mesh 1, are respectively plotted in Figs.16a and b. The maps of maximum principal stress carried out with Mesh 2 are respectively plotted in Figs.16c and d. These maps of stress are plotted in the deformed configuration and they show almost coincident results, both in terms of stress and in terms of crack path. Moreover, it is noteworthy that the crack paths numerically represented in the Figures overlap area of crack experimentally observed and highlighted in Fig.14.

6 | CONCLUSIONS

The paper proposes an approach for modelling a crack propagation at the inter-element interface of Hybrid Equilibrium Elements, which is not affected by mesh dependency neither in terms of size, nor in terms of side orientation. The HEE formulation gives a solution of the two-dimensional elasto-static problems, which strongly satisfy the continuum equilibrium equations in the whole domain and makes it possible to implicitly embed an extrinsic interface at every element side with neither additional degrees of freedom nor addition nodes. Interface is embedded only at sides where crack growth criterion is attained and is modelled by an extrinsic cohesive model, developed in the rigorous thermodynamic framework of damage mechanics, which produces a bilinear traction separation law with initially rigid behaviour. The crack growth criterion is based on the maximum principal stress rule with direction of propagation orthogonal to the principal stress direction, which generally does not coincides to any element side. The last issue requires the remeshing of the elements ahead the crack tip with an adaptive orientation of the element sides to the direction of crack propagation. An extrinsic interface is eventually embedded to the element side aligned to the crack growth direction. The direction of propagation of the embedded crack in a HEE is fixed at its activation and is no longer amended thereafter.

A modified crack growth criterion is also proposed in order to overcome the numerical instability encountered in the direction of crack propagation and arising from the state of stress at the crack tip of the cohesive zone. In fact, due to the increase of the second principal stress, an almost hydrostatic state of stress at the crack tip of the cohesive zone generates uncertainty and instability in the direction of crack propagation. The proposed modified crack growth criterion assumes as angle of the direction

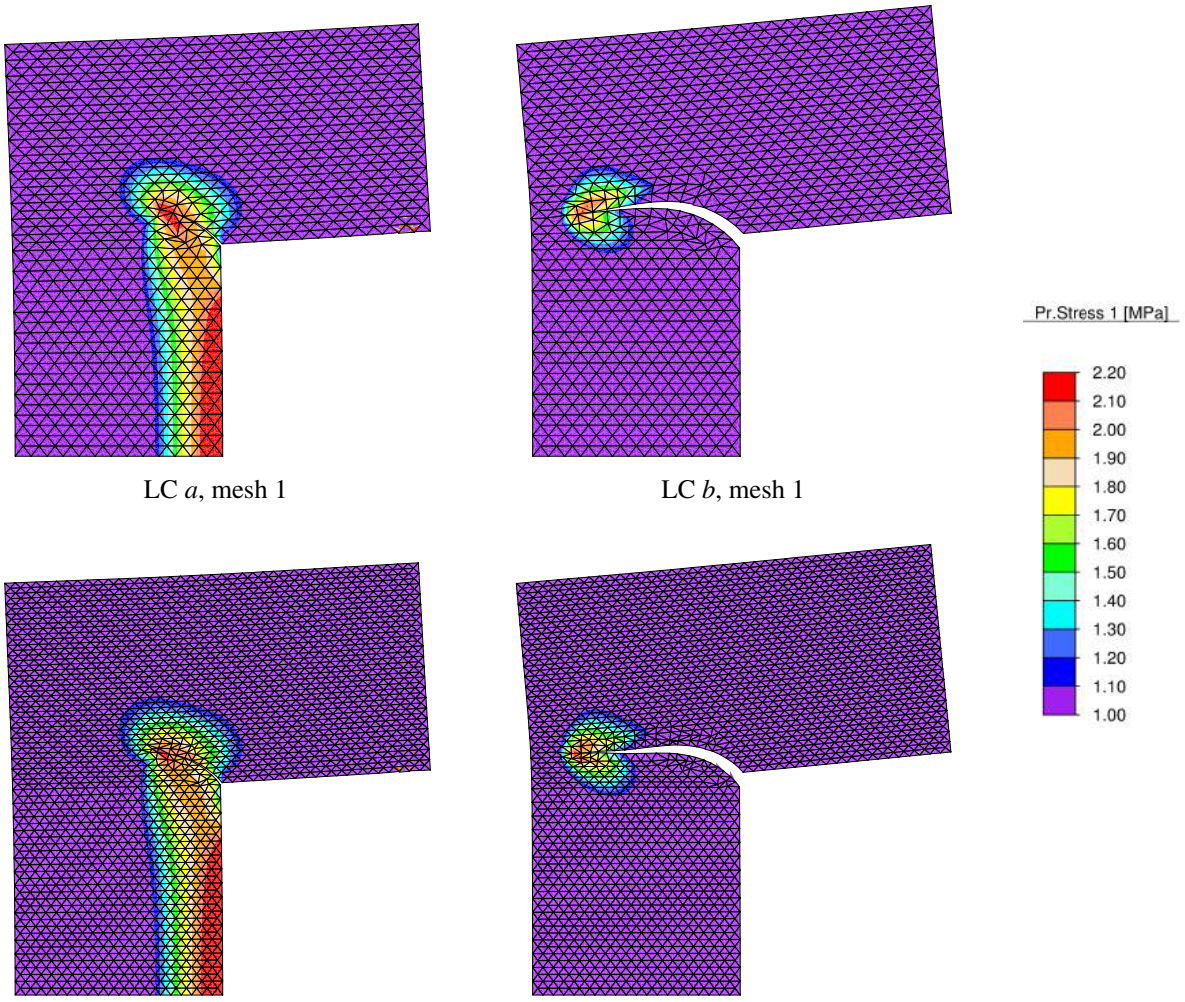

FIGURE 13 Contour of maximum principal stress carried out by the numerical simulation of the LSCP with mesh 1 and with mesh 2, at the two loading conditions (LCs *a* and *b*) pointed out in Fig.12

of propagation a weighted value between the angle of the previous branch of crack and the angle of the maximum principal stress. The weight parameter is given as a function of the two principal stresses.

The proposed HEE formulation, with embedded extrinsic interface and remeshing with adaptive orientation of the element sides have been implemented in a finite element code and the numerical simulations of three well known crack propagation problems have been carried out with different mesh sizes, mesh orientations and stress orders. The numerical results clearly shows that numerical solutions of crack propagation problems are not significantly affected by a mesh dependency both in terms of crack path and load-displacement response. However, the problem of the maximum size of element that can be used with a sufficiently good approximation of stress field and overall non-linear response is not faced in the present paper and is considered a relevant aspect for future insights. The numerical results are compared to experimental data and to the numerical results obtained by different approaches already available in literature, showing very good agreement.

Future developments of the proposed model could be: the modelling of frictionless and frictional contact under crack closing and the formulation of the HEE for the dynamic analysis of crack and fragmentation problems.

□

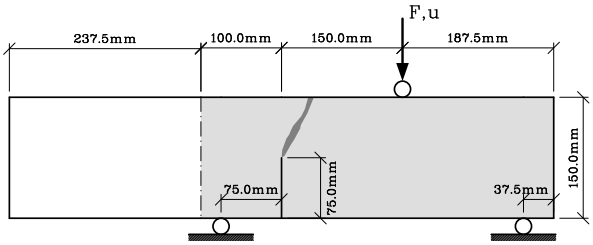

FIGURE 14 Set-up and sizes of the single-edge notched concrete beam. The zone in dark grey highlights the region where crack is experimentally observed[73]. The light grey area is discretized in HEE. Thickness is $t = 50\,\text{mm}$.

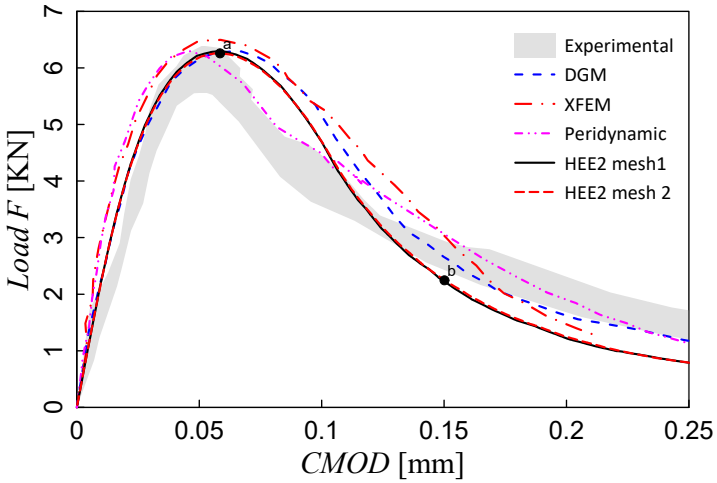

FIGURE 15 Numerical responses of the SENB, in terms of CMOD and force F. The numerical results are compared to the experimental data reported in Ref.[73] and to others numerical solutions[54,74,69]. The labels a and b point out respectively the maximum load conditions and the loading condition corresponding to CMOD value of 0.15 mm.

APPENDIX

A HIGH-ORDER STATIC COEFFICIENT MATRICES

The two-dimensional stress components are defined as functions of the Cartesian coordinates in Eqs.(2-4) for the quadratic formulation and are represented in Eq.(5) in the Voigt notation. The element stress modelling matrix $\mathbf{S}_e(\mathbf{x})$ and the vector $\mathbf{a}_e$ of the *generalized stress* variables for the quadratic formulation ($n_s = 2$, $n_a = 12$) are

$$\mathbf{S}_e(\mathbf{x}) = \begin{bmatrix} 1 & y & y^2 & 0 & 0 & 0 & 0 & 0 & -x & -x^2/2 & 0 & -2xy \\ 0 & 0 & 0 & 1 & x & x^2 & 0 & -y & 0 & -y^2/2 & -2xy & 0 \\ 0 & 0 & 0 & 0 & 0 & 0 & 1 & x & y & xy & x^2 & y^2 \end{bmatrix} \tag{A1}$$

$$\mathbf{a}_e = \begin{bmatrix} a_1 & a_2 & a_3 & a_4 & a_5 & a_6 & a_7 & a_8 & a_9 & a_{10} & a_{11} & a_{12} \end{bmatrix}^T, \tag{A2}$$

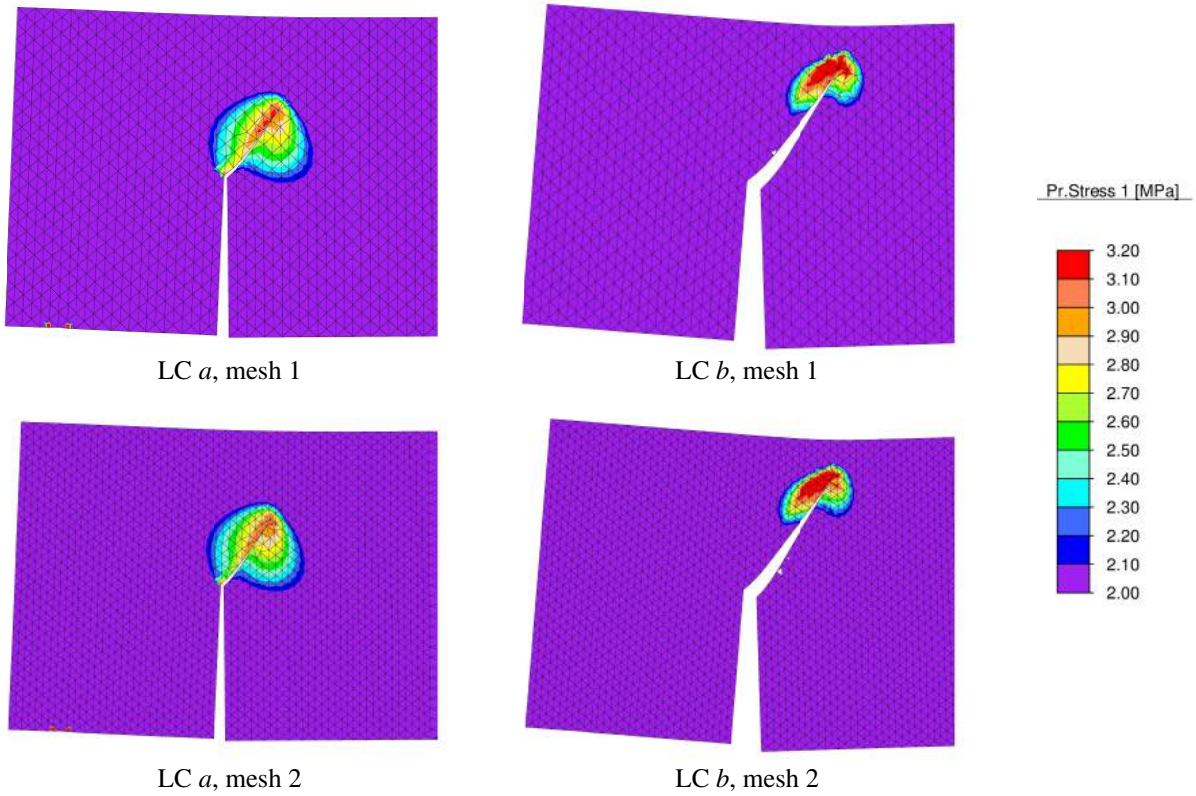

FIGURE 16 Contour of maximum principal stress carried out by the numerical simulation of the SENB with mesh 1 and with mesh 2, at the two loading conditions (LC *a* and *b*) pointed out in Fig.15

for the cubic formulation ($n_s = 3$, $n_a = 18$), and

$$\mathbf{S}_e(\mathbf{x}) = \begin{bmatrix} 1 & y & y^2 & y^3 & 0 & 0 & 0 & 0 & 0 & 0 & -x & -x^2/2 & 0 & -2xy & -x^3/3 & -x^2y & 0 & -3xy^2 \\ 0 & 0 & 0 & 0 & 1 & x & x^2 & x^3 & 0 & -y & 0 & -y^2/2 & -2xy & 0 & -xy^2 & -y^3/3 & -3x^2y & 0 \\ 0 & 0 & 0 & 0 & 0 & 0 & 0 & 0 & 1 & x & y & xy & x^2 & y^2 & x^2y & xy^2 & x^3 & y^3 \end{bmatrix} \tag{A3}$$

$$\mathbf{a}_e = \begin{bmatrix} a_1 & a_2 & a_3 & \dots & a_{16} & a_{17} & a_{18}, \end{bmatrix}^T \tag{A4}$$

and for the quartic formulation ($n_s = 4$, $n_a = 25$)

$$\mathbf{S}_e(\mathbf{x}) = \begin{bmatrix} 1 & y & y^2 & y^3 & y^4 & 0 & 0 & 0 & 0 & 0 & 0 & 0 & -x & -x^2/2 & 0 & -2xy & -x^3/3 \\ 0 & 0 & 0 & 0 & 0 & 1 & x & x^2 & x^3 & x^4 & 0 & -y & 0 & -y^2/2 & -2xy & 0 & -xy^2 \\ 0 & 0 & 0 & 0 & 0 & 0 & 0 & 0 & 0 & 0 & 1 & x & y & xy & x^2 & y^2 & x^2y \\ -x^2y & 0 & -3xy^2 & -x^4/4 & -2/3x^3y & -3/2x^2y^2 & 0 & -4y^3x \\ -y^3/3 & -3x^2y & 0 & -3/2x^2y^2 & -2/3y^3x & -y^4/4 & -4x^3y & 0 \\ xy^2 & x^3 & y^3 & x^3y & x^2y^2 & xy^3 & x^4 & y^4 \end{bmatrix} \tag{A5}$$

$$\mathbf{a}_e = \begin{bmatrix} a_1 & a_2 & a_3 & \dots & a_{23} & a_{24} & a_{25}, \end{bmatrix}^T . \tag{A6}$$

ACKNOWLEDGMENT

A grant from the Ministry for University and Research (MUR) for PRIN 2022, project No. 2022P7PF8J-002, LAttice STructures for Energy aBsorption: advanced numerical analysis and optimal design (LASTEB) is gratefully acknowledged.

CONFLICT OF INTEREST

The authors declare no potential conflict of interests.

DATA AVAILABILITY

The datasets generated and analysed during the current study are available from the corresponding author on reasonable request.

References

1. Polizzotto C. Unified thermodynamic framework for nonlocal/gradient continuum theories. *European Journal of Mechanics, A/Solids* 2003; 22(5): 651-668.

2. Benvenuti E, Borino G, Tralli A. A thermodynamically consistent nonlocal formulation for damaging materials. *European Journal of Mechanics, A/Solids* 2002; 21(4): 535-553. doi: 10.1016/S0997-7538(02)01220-2

3. Borino G, Failla B, Parrinello F. A symmetric nonlocal damage theory. *International Journal of Solids and Structures* 2003; 40(13-14): 3621-3645.

4. Verhoosel CV, de Borst R. A phase-field model for cohesive fracture. *International Journal for Numerical Methods in Engineering* 2013; 96(1): 43-62.

5. Miehe C, Welschinger F, Hofacker M. Thermodynamically consistent phase-field models of fracture: Variational principles and multi-field FE implementations. *International Journal for Numerical Methods in Engineering* 2010; 83(10): 1273-1311. doi: https://doi.org/10.1002/nme.2861

6. Simo J, Oliver J, Armero F. An Analysis of Strong Discontinuities induced by strain softening in rate-independent inelastic solids. *Computational Mechanics* 1993; 12: 277-296. doi: 10.1007/BF00372173

7. Jirasek M. Comparative study on finite elements with embedded discontinuities. *Computer Methods in Applied Mechanics and Engineering* 2000; 188: 307-330.

8. Oliver J, Huespe AE. Theoretical and computational issues in modelling material failure in strong discontinuity scenarios. *Computer Methods in Applied Mechanics and Engineering* 2004; 193(27): 2987 - 3014. Computational Failure Mechanics for Geomaterialsdoi: https://doi.org/10.1016/j.cma.2003.08.007

9. Huespe A, Oliver J. *Crack Models with Embedded Discontinuities*: 99–159; Vienna: Springer Vienna . 2011.

10. Moës N, Dolbow J, Belytschko T. A finite element method for crack growth without remeshing. *International Journal for Numerical Methods in Engineering* 1999; 46(1): 131-150. doi: 10.1002/(SICI)1097-0207(19990910)46:1<131::AID-NME726>3.0.CO;2-J

11. Zi G, Belytschko T. New crack-tip elements for XFEM and applications to cohesive cracks. *International Journal for Numerical Methods in Engineering* 2003; 57(15): 2221-2240. doi: 10.1002/nme.849

12. Fries TP, Belytschko T. The extended/generalized finite element method: An overview of the method and its applications. *International Journal for Numerical Methods in Engineering* 2010; 84(3): 253-304. doi: https://doi.org/10.1002/nme.2914

13. Oliver J, Huespe A, Sánchez PJ. A comparative study on finite elements for capturing strong discontinuities: E-FEM vs X-FEM. *Computer Methods in Applied Mechanics and Engineering* 2006; 195(37-40): 4732-4752.

14. Erdogan F, Sih G. On the crack extension in plates under plane loading and transverse shear. *Journal of Fluids Engineering, Transactions of the ASME* 1963; 85(4): 519 – 525. doi: 10.1115/1.3656897

15. Hussain M, Pu S, Underwood J. Strain energy release rate for a crack under combined mode I and mode II. *Fracture Analysis ASTM* 1974; 560: 2-28.

16. Rice JR. A Path Independent Integral and the Approximate Analysis of Strain Concentration by Notches and Cracks. *Journal of Applied Mechanics* 1968; 35(2): 379-386. doi: 10.1115/1.3601206

17. Li F, Shih C, Needleman A. A comparison of methods for calculating energy release rates. *Engineering Fracture Mechanics* 1985; 21(2): 405-421. doi: https://doi.org/10.1016/0013-7944(85)90029-3

18. Dugdale D. Yielding of Steel Sheets Containing Slits. *J. Mech. Phys. Solids.* 1960; 8: 100-104.

19. Barenblatt G. The mathematical theory of equilibrium cracks in brittle fracture. *Advances in Applied Mechanics* 1962; 7: 55-129.

20. Gdoutos E. *Fracture Mechanics. An introduction*. Kluver Academic Publishers . 1993.

21. Corigliano A, Allix O. Some aspects of interlaminar degradation in composites. *Comp. Meth. Appl. Mech. Eng.* 2000; 185(2-4): 203-224.

22. Spada A, Giambanco G, Rizzo P. Damage and plasticity at the interfaces in composite materials and structures. *Comp. Meth. Appl. Mech. Eng.* 2009; 198(49-52): 3884-3901.

23. Alfano G, Crisfield M. Finite element interface models for the delamination analysis of laminated composites: Mechanical and computational issues. *International Journal for Numerical Methods in Engineering* 2001; 50(7): 1701-1736.

24. Parrinello F, Marannano G, Borino G. A thermodynamically consistent cohesive-frictional interface model for mixed mode delamination. *Engineering Fracture Mechanics* 2016; 153: 61-79. doi: 10.1016/j.engfracmech.2015.12.001

25. Parrinello F, Borino G. Non associative damage interface model for mixed mode delamination and frictional contact. *European Journal of Mechanics / A Solids* 2019; 76: 108-122.

26. Parrinello F, Failla B, Borino G. Cohesive-frictional interface constitutive model. *International Journal of Solids and Structures* 2009; 46(13): 2680-2692.

27. Mosler J, Scheider I. A thermodynamically and variationally consistent class of damage-type cohesive models. *J. Mech. Physics Solids* 2011; 59(8): 1647-1668.

28. Guiamatsia I, Nguyen G. A thermodynamics-based cohesive model for interface debonding and friction. *International Journal of Solids and Structures* 2014; 51(3-4): 647-659.

29. Serpieri R, Sacco E, Alfano G. A thermodynamically consistent derivation of a frictional-damage cohesive-zone model with different mode i and mode II fracture energies. *Eur. J. Mech., A/Solids* 2015; 49: 13-25.

30. Parrinello F, Borino G. Integration of finite displacement interface element in reference and current configurations. *Meccanica* 2018; 53(6): 1455-1468.

31. Simone A. Partition of unity-based discontinuous elements for interface phenomena: Computational issues. *Communications in Numerical Methods in Engineering* 2004; 20(6): 465-478. doi: 10.1002/cnm.688

32. Mergheim J, Kuhl E, Steinmann P. A hybrid discontinuous Galerkin/interface method for the computational modelling of failure. *Communications in Numerical Methods in Engineering* 2004; 20(7): 511-519. doi: 10.1002/cnm.689

33. Nitsche J. Über ein Variationsprinzip zur Lösung von Dirichlet-Problemen bei Verwendung von Teilräumen, die keinen Randbedingungen unterworfen sind. *Abhandlungen aus dem Mathematischen Seminar der Universität Hamburg* 1971; 36(1): 9–15. doi: 10.1007/bf02995904

34. Nguyen VP, Nguyen CT, Bordas S, Heidarpour A. Modelling interfacial cracking with non-matching cohesive interface elements. *Computational Mechanics* 2016; 58(5): 731-746. doi: 10.1007/s00466-016-1314-y

35. Truster TJ, Masud A. A Discontinuous/continuous Galerkin method for modeling of interphase damage in fibrous composite systems. *Computational Mechanics* 2013; 52(3): 499–514. doi: 10.1007/s00466-012-0827-2

36. Benedetti I, Aliabadi MH. A three-dimensional cohesive-frictional grain-boundary micromechanical model for intergranular degradation and failure in polycrystalline materials. *Computer Methods in Applied Mechanics and Engineering* 2013; 265: 36-62. doi: 10.1016/j.cma.2013.05.023

37. Benedetti I, Gulizzi V, Milazzo A. Grain-boundary modelling of hydrogen assisted intergranular stress corrosion cracking. *Mechanics of Materials* 2018; 117: 137-151. doi: 10.1016/j.mechmat.2017.11.001

38. Versino D, Mourad HM, Dávila CG, Addessio FL. A thermodynamically consistent discontinuous Galerkin formulation for interface separation. *Composite Structures* 2015; 133: 595 - 606. doi: https://doi.org/10.1016/j.compstruct.2015.07.080

39. Noels L, Radovitzky R. An explicit discontinuous Galerkin method for non-linear solid dynamics: Formulation, parallel implementation and scalability properties. *International Journal for Numerical Methods in Engineering* 2008; 74(9): 1393-1420. doi: 10.1002/nme.2213

40. Radovitzky R, Seagraves A, Tupek M, Noels L. A scalable 3D fracture and fragmentation algorithm based on a hybrid, discontinuous Galerkin, cohesive element method. *Computer Methods in Applied Mechanics and Engineering* 2011; 200(1-4): 326-344. doi: 10.1016/j.cma.2010.08.014

41. Lorentz E. A mixed interface finite element for cohesive zone models. *Computer Methods in Applied Mechanics and Engineering* 2008; 198(2): 302 - 317. doi: https://doi.org/10.1016/j.cma.2008.08.006

42. Parrinello F. Hybrid equilibrium element with interelement interface for the analysis of delamination and crack propagation problems. *International Journal for Numerical Methods in Engineering* 2020. doi: 10.1002/nme.6531

43. Fraeijs de Veubeke B. *Stress Analysis*. Zienkiewicz O.C., Holister G.S. (eds), Chapter 9. Wiley: London . 1965.

44. Moitinho de Almeida JP, Teixeira de Freitas JA. An alternative approach to the formulation of hybrid equilibrium finite elements. *Computers and Structures* 1991; 40: 1043 - 1047.

45. Almeida Pereira OJB. Hybrid equilibrium hexahedral elements and super-elements.. *Commun. Numer. Meth. Engng* 2008; 24: 157 - 165.

46. Moitinho de Almeida J, Almeida Pereira O. A set of hybrid equilibrium finite element models for the analysis of three-dimensional solids. *International Journal for Numerical Methods in Engineering* 1996; 39(16): 2789-2802.

47. Kempeneers M, Debongnie JF, Beckers P. Pure equilibrium tetrahedral finite elements for global error estimation by dual analysis. *International Journal for Numerical Methods in Engineering* 2010; 81: 513 - 536.

48. Almeida Pereira OJB, Moitinho de Almeida J, Maunder EAW. Adaptive methods for hybrid equilibrium finite element models. *Computer Methods in Applied Mechanics and Engineering* 1999; 176: 19 - 39.

49. Parrinello F, Borino G. Hybrid equilibrium element with high-order stress fields for accurate elastic dynamic analysis. *International Journal for Numerical Methods in Engineering* 2021; 122(21): 6308 – 6340. doi: 10.1002/nme.6793

50. Pian THH. State-of-the-art development of hybrid/mixed finite element method. *Fin. Elem. in Analysis and Design* 1995; 21: 5 - 20.

51. Parrinello F. Restraining approach for the spurious kinematic modes in hybrid equilibrium element. *Computational Mechanics* 2013; 52(4): 885-901. doi: 10.1007/s00466-013-0851-x

52. Maunder EAW, Moitinho de Almeida JP, Ramsay ACA. A general formulation of equilibrium macro-elements with control of spurious kinematic modes: the exorcism of an old curse. *International Journal For Numerical Methods In Engineering* 1996; 39: 3175 - 3194.

53. Nguyen VP. Discontinuous Galerkin/extrinsic cohesive zone modeling: Implementation caveats and applications in computational fracture mechanics. *Engineering Fracture Mechanics* 2014; 128(C): 37-68. doi: 10.1016/j.engfracmech.2014.07.003

54. Hirmand MR, Papoulia KD. A continuation method for rigid-cohesive fracture in a discontinuous Galerkin finite element setting. *International Journal for Numerical Methods in Engineering* 2018; 115(5): 627-650. doi: 10.1002/nme.5819

55. Parrinello F, Gulizzi V, Benedetti I. A computational framework for low-cycle fatigue in polycrystalline materials. *Computer Methods in Applied Mechanics and Engineering* 2021; 383: 113898. doi: https://doi.org/10.1016/j.cma.2021.113898

56. Parrinello F, Benedetti I. A coupled plasticity-damage cohesive-frictional interface for low-cycle fatigue analysis. *International Journal of Mechanical Sciences* 2022; 224: 107298. doi: https://doi.org/10.1016/j.ijmecsci.2022.107298

57. Nuismer R. An energy release rate criterion for mixed mode fracture. *International Journal of Fracture* 1975; 11(2): 245 – 250. doi: 10.1007/BF00038891

58. Sih G. Strain-energy-density factor applied to mixed mode crack problems. *International Journal of Fracture* 1974; 10(3): 305 – 321. doi: 10.1007/BF00035493

59. Bažant ZP, Lin F. Nonlocal Smeared Cracking Model for Concrete Fracture. *Journal of Structural Engineering* 1988; 114(11): 2493-2510. doi: 10.1061/(ASCE)0733-9445(1988)114:11(2493)

60. Jirásek M, Zimmermann T. Rotating Crack Model with Transition to Scalar Damage. *Journal of Engineering Mechanics* 1998; 124(3): 277-284. doi: 10.1061/(ASCE)0733-9399(1998)124:3(277)

61. Jirásek M, Zimmermann T. Embedded crack model. Part II: combination with smeared cracks. *International Journal for Numerical Methods in Engineering* 2001; 50(6): 1291-1305. doi: https://doi.org/10.1002/1097-0207(20010228)50:6<1291::AID-NME12>3.0.CO;2-Q

62. Chen L, Borst dR. Cohesive fracture analysis using Powell-Sabin B-splines. *International Journal for Numerical and Analytical Methods in Geomechanics* 2019; 43(2): 625-640. doi: https://doi.org/10.1002/nag.2882

63. Zienkiewicz OC, Taylor . *The Finite Element Method. 5th Edition*. Butterworth-Heinemann Press . 2000.

64. Maunder EAW, Moitinho de Almeida JP. Hybrid-equilibrium elements with control of spurious kinematic modes.. *Computer Assisted Mechanics and Engineering Sciences* 1997; 4: 587-605.

65. Wang L, Zhong H. A traction-based equilibrium finite element free from spurious kinematic modes for linear elasticity problems. *International Journal for Numerical Methods in Engineering* 2014; 99(10): 763-788. doi: 10.1002/nme.4701

66. Maunder EAW, Moitinho de Almeida JP. The stability of stars of triangular equilibrium plate elements.. *International Journal for Numerical Methods in Engineering* 2009; 77: 922 - 968.

67. Li Y, Zimmerman T. Numerical evaluation of the rotating crack model. *Computers & Structures* 1998; 69(4): 487-497. doi: https://doi.org/10.1016/S0045-7949(98)00118-7

68. Alebrahim R, Thamburaja P, Srinivasa A, Reddy J. A robust Moore–Penrose pseudoinverse-based static finite-element solver for simulating non-local fracture in solids. *Computer Methods in Applied Mechanics and Engineering* 2023; 403: 115727. doi: https://doi.org/10.1016/j.cma.2022.115727

69. Alebrahim R, Marfia S. A fast adaptive PD-FEM coupling model for predicting cohesive crack growth. *Computer Methods in Applied Mechanics and Engineering* 2023; 410: 116034. doi: https://doi.org/10.1016/j.cma.2023.116034

70. Winkler B. *Traglastuntersuchungen von unbewehrten und bewehrten Betonstrukturen auf der Grundlage eines objektiven Werkstoffgesetzes für Beton.* Phd thesis. University of Innsbruck, Austria, 2001.

71. Winkler B, Hofstetter G, Lehar H. Application of a constitutive model for concrete to the analysis of a precast segmental tunnel lining. *International Journal for Numerical and Analytical Methods in Geomechanics* 2004; 28(7-8): 797–819.

72. Mosler J, Meschke G. Embedded crack vs. smeared crack models: a comparison of elementwise discontinuous crack path approaches with emphasis on mesh bias. *Computer Methods in Applied Mechanics and Engineering* 2004; 193(30): 3351-3375. doi: https://doi.org/10.1016/j.cma.2003.09.022

73. Gálvez J, Elices M, Guinea G, Planas J. Mixed mode fracture of concrete under proportional and nonproportional loading. *International Journal of Fracture* 1998; 94(3): 267-284. doi: 10.1023/A:1007578814070

74. Areias P, Belytschko T. Analysis of three-dimensional crack initiation and propagation using the extended finite element method. *International Journal for Numerical Methods in Engineering* 2005; 63(5): 760-788. doi: 10.1002/nme.1305